

# Modeling Antarctic ice shelf basal melt patterns using the one-Layer Antarctic model for Dynamical Downscaling of Ice–ocean Exchanges (LADDIE v1.0)

Erwin Lambert<sup>1</sup>, André Jüling<sup>1</sup>, Roderik S. W. van de Wal<sup>2,3</sup>, and Paul R. Holland<sup>4</sup>

<sup>1</sup>Royal Netherlands Meteorological Institute (KNMI), De Bilt, The Netherlands

<sup>2</sup>Institute for Marine and Atmospheric Research Utrecht (IMAU), Utrecht University, Utrecht, The Netherlands

<sup>3</sup>Department of Physical Geography, Utrecht University, Utrecht, The Netherlands

<sup>4</sup>British Antarctic Survey, Cambridge, UK

**Correspondence:** Erwin Lambert (erwin.lambert@knmi.nl)

**Abstract.** A major source of uncertainty in future sea-level projections is the ocean-driven basal melt of Antarctic ice shelves. Whereas ice sheet models require a ~~kilometer-scale~~ kilometre-scale resolution to realistically resolve ice shelf stability and grounding line migration, global or regional 3D ocean models are computationally too expensive to produce basal melt forcing fields at this resolution on long time scales. To bridge this resolution gap, we introduce the 2D numerical model LADDIE (one-  
5 Layer Antarctic model for Dynamical Downscaling of Ice–ocean Exchanges) which allows for the computationally efficient modeling of ~~basal melt rates~~ detailed basal melt fields. The model is ~~flexible, available open source~~ and can be ~~forced with output from coarse 3D ocean models or with vertical profiles of offshore temperature and salinity. In this study, we describe the model equations and numerics. To illustrate and validate the model performance, we apply the model to two test cases: the small Crosson–Dotson~~ applied easily to different geometries or different ocean forcing. The aim of this study is threefold: to introduce  
10 the model to the community; to demonstrate its application and performance in two use cases; and to describe and interpret new basal melt patterns simulated by this model. The two use cases are the small Crosson–Dotson Ice Shelf in the warm Amundsen Sea region, and the large ~~Filchner–Ronne~~ Filchner–Ronne Ice Shelf in the cold Weddell Sea. At ice-shelf wide scales, LADDIE reproduces observed patterns of basal ~~melt and freezing that are also well reproduced by 3D ocean models~~ melting and freezing in warm and cold environments without the need to retune parameters. At scales of 0.5–5 km, which are typically unresolved by  
15 3D ocean models and poorly constrained by observations, LADDIE produces plausible basal melt patterns. Most significantly, the simulated basal melt patterns are physically consistent with the applied ice shelf topography. These patterns are governed by the topographic steering and Coriolis deflection of meltwater flows, two processes that are poorly represented in basal melt parameterisations. The ~~kilometer-scale~~ kilometre-scale melt patterns simulated by LADDIE include enhanced melt rates in grounding zones and basal channels, ~~in some shear margins, and nearby grounding lines~~ and enhanced melt or freezing  
20 in shear margins. As these regions are critical for ice shelf stability, we conclude that LADDIE can provide detailed basal melt patterns at the essential resolution that ice sheet models require. The physical consistency between the applied geometry and the simulated basal melt fields indicates that LADDIE can play a valuable role in the development of coupled ice–ocean modeling.

# 1 Introduction

25 Sea-level projections come with a large uncertainty ~~in particular those beyond 2100~~ (Oppenheimer et al., 2019; Fox-Kemper et al., 2021). A major component of this uncertainty is the ocean-driven basal melt of Antarctic ice shelves (Seroussi et al., 2020). Basal melt is a critical process that determines the state and fate of ice shelves. Increased basal melt can lead to a thinning and weakening of ice shelves, which in turn reduces their buttressing effect on the ice flow of grounded ice to the ocean (e.g. Gudmundsson et al., 2019; Sun et al., 2020). Basal melt rates must thus be modeled accurately in order to simulate  
30 ice sheet dynamics and future sea-level projections (Goldberg et al., 2019). The modeling is obstructed, however, by the high computational cost of three-dimensional ocean models when configured at a high resolution. As a consequence, modeled basal melt rates are typically provided at a substantially coarser resolution than that at which ice sheet model simulations are performed. In this study, we present a new two-dimensional basal melt model, LADDIE (one-Layer Antarctic model for Dynamical Downscaling of Ice-ocean Exchanges). This model simulates the quasi-horizontal flow of the meltwater layer  
35 beneath the ice shelf base. Using this model, one can simulate (sub-)kilometer-kilometre basal melt rates ~~can be simulated~~ under reasonable computational cost.

Basal melt is strongly determined by the ocean dynamics in the upper ocean layer below the ice shelves. At the ice shelf base, melting produces a flux of fresh and cold meltwater ~~is produced~~. Due to the salinity-dominated density contrast with the surrounding seawater, this fresher meltwater rises along the slope of the ice shelf base toward the ice shelf front. The velocity  
40 of this meltwater flow, relative to the ~~presumed stagnant~~ ocean beneath, induces shear-driven turbulence. This turbulence maintains a net transfer of heat ~~in salt and mass~~ and salt from the cavity waters toward the upper ocean layer. The buoyancy-driven transport and downstream modification of the meltwater is typically referred to as plume dynamics (Jenkins, 1991). Due to the turbulence-driven heat import from ~~ambient~~ deeper cavity waters, the upper ocean layer is typically warmer than the local pressure-melting point. As a consequence, the plume dynamics maintain basal melt, the transport of meltwater, and a net  
45 overturning circulation. It is these dynamics of the upper ocean layer that are simulated by LADDIE.

Observations from remote sensing products have revealed clear, spatially heterogeneous patterns in basal melt rates. Compared to the ice shelf average values, basal melt rates are enhanced in specific regions. Along all Antarctic ice shelves, enhanced melt rates are observed in the deep grounding zones near the deepest parts of the grounding line (Rignot and Jacobs, 2002; Rignot et al., 2013). Detailed observations of individual grounding zones have shown that local basal melt rates can vary by  
50 an order of magnitude ~~at~~ over horizontal distances of ~~kilometers~~ kilometres (Dutrieux et al., 2013; Khazendar et al., 2016; Marsh et al., 2016). Stretching from the grounding zones to the ice-shelf front, elevated basal melt rates are also observed in narrow topographic channels in both warm and cold regions (Alley et al., 2016; Berger et al., 2017). With the exception of some very wide channels (Gourmelen et al., 2017), most have a characteristic width of a ~~kilometer~~ kilometre (Zeising et al., 2022). These basal channels ~~have a preference for aligning~~ are commonly aligned along topographic boundaries and margins  
55 of high ice-velocity shear (Alley et al., 2019). In these shear margins, locally enhanced basal melt can initiate ice shelf damage (Lhermitte et al., 2020). Altogether, these observations have shown that basal melt rates vary spatially at scales of ~~kilometers~~ kilometres across ice shelves in both warm and cold regions.

The ice mass loss contributing to sea-level rise is simulated by numerical ice sheet models. These models require basal melt rates as an external forcing (Seroussi et al., 2020). In various studies, the stability of modeled ice sheets was found to be most sensitive to basal melt in specific regions. ~~The basal melt regions inducing the strongest ice mass loss were found to be~~ , in particular grounding zones (Reese et al., 2018b; Goldberg et al., 2019) and shear zones (Goldberg et al., 2019; Feldmann et al., 2022). Moreover, locally enhanced basal melt in grounding zones is identified as a necessary ingredient to reproduce the observed grounding line retreat of the Smith glacier (Lilien et al., 2019). In a state-of-the-art ice sheet model, basal melt within a ~~kilometer-scale~~ kilometre-scale distance from the grounding line ~~most strongly affected the~~ was identified as the dominant process governing ice sheet stability (Seroussi and Morlighem, 2018). ~~In a coupled~~ Coupled ice–ocean ~~simulation,~~ simulations indicate that enhanced basal melt rates in channels ~~along the western boundaries led to a reduction in buttressing~~ have a limited impact on ice mass loss when aligned in the center of an ice shelf (Goldberg and Holland, 2022), but can have a large impact when aligned along a western boundary (Jordan et al., 2018). These studies together suggest that the spatial pattern of basal melt is as important as average melt rates to the ice-sheet response. In particular, an accurate basal melt forcing is required in the regions where observations indicate locally enhanced basal melt rates; ~~these are the~~ : grounding zones, basal channels, and shear zones. The realistic simulation of these ~~kilometer-scale~~ kilometre-scale basal melt patterns is therefore a key goal for ocean and ice modelers.

Basal melt rates can be simulated using 3D ocean models by explicitly resolving the circulation within ice shelf cavities (e.g., Mathiot et al., 2017). These models are well-suited to simulate the exchange of heat between the deep ocean, the continental shelf, and the ice shelf cavities. This heat exchange is governed by, among other drivers, the Antarctic Slope Current (Thompson et al., 2018; Nakayama et al., 2021), bathymetric troughs (e.g., Wåhlin et al., 2021), and dense water formation (Morrison et al., 2020). A range of 3D models have performed well in representing the overall heat transport onto the continental shelf and into ice shelf cavities (e.g., Kimura et al., 2017; Nakayama et al., 2019; Moorman et al., 2020; Naughten et al., 2022). However, 3D ocean models are computationally too expensive to resolve ~~kilometer-scale processes~~ kilometre-scale processes in the large domains and long simulations needed to conduct climate change projections (Hewitt et al., 2022). These models ~~can only be feasibly~~ are typically configured globally at a resolution of  $0.25^\circ$  ( $\approx 7.5$  km near Antarctica) (e.g., Mathiot et al., 2017; Pelletier et al., 2022). At such a coarse resolution, ocean models are clearly unable to reproduce ~~kilometer-scale~~ kilometre-scale features such as basal melt channels. For example, the coupled United Kingdom Earth System Model includes an ocean model at  $1^\circ$  resolution ( $\approx 30$  km near Antarctica) and an ice sheet model with 2 km resolution at the Antarctic grounding line (Smith et al., 2021; Siahhaan et al., 2022). This high ice-sheet model resolution is required in particular in the grounding zone to reliably model the evolution of the grounding line (Schoof, 2007). The example illustrates the large resolution gap between the basal melt rates that ocean models can provide, and that which ice sheet models require.

In part due to this resolution gap, numerical ice sheet models are typically forced with parameterised basal melt rates (Seroussi et al., 2020). These parameterisations are either linear or quadratic scalings of offshore temperatures and salinities ~~(Favier et al., 2019)~~ (e.g., Favier et al., 2019), or built upon (quasi-)one-dimensional flow descriptions of meltwater below the ice shelf (Reese et al., 2018a; Lazeroms et al., 2019; Pelle et al., 2019). The (quasi-)one-dimensional parameterisations may reasonably resolve enhanced melt rates in the deeper grounding zones (Favier et al., 2019; Burgard et al., 2022). Yet these

parameterisations require assumptions ~~on about~~ the horizontal flow field of meltwater plumes (Favier et al., 2019). As a consequence, the parameterised melt patterns do not ~~account for explicitly model~~ the Coriolis deflection of this flow field (Holland and Feltham, 2006). In addition, these parameterisations do ~~at most partly account for not explicitly model~~ the topographic steering of the subshef flow field, which is crucial to resolve the enhanced basal melt within basal channels (Gladish et al., 2012; Millgate et al., 2013; Alley et al., 2019). Whilst ~~being able to provide providing~~ basal melt rates at a low computational cost, these parameterisations are thus ill-equipped to produce detailed spatial basal melt patterns.

In order to simulate realistic, high-resolution basal melt patterns, we here present the 2D model LADDIE (one-Layer Antarctic model for Dynamical Downscaling of Ice–ocean Exchanges). The model is built upon previous 2D (plan view) models of the upper ocean below ice shelves (Holland and Feltham, 2006), which have been applied to the ~~Filchner-Ronne Filchner-Ronne~~ (Holland et al., 2007), Larsen (Holland et al., 2009) and Pine Island (Payne et al., 2007) ice shelves with smooth ice shelf topographies. LADDIE is specifically designed to simulate basal melt rates that are consistent with ~~an~~ unsmoothed ice shelf topography. The consistency of the basal melt rates with the ice shelf topography makes the model suitable for studies investigating ~~kilometer-scale kilometre-scale~~ ice–ocean feedbacks, such as within basal channels (Gladish et al., 2012; Sergienko, 2013; Alley et al., 2019). By resolving the 2D flow field and its Coriolis deflection and topographic steering, the model can simulate the important basal melt rates along topographic boundaries and within shear zones (Jordan et al., 2018; Feldmann et al., 2022). As the model can be configured at a ~~sub-kilometer sub-kilometre~~ resolution, it can also simulate detailed basal melt rates in the important region near grounding lines (Seroussi and Morlighem, 2018). The 2D configuration prevents the model from explicitly resolving processes like turbulence and the barotropic and overturning circulations in the cavity; these processes are approximated or parameterised. The model can either be forced with 3D ocean model output, when cavities are explicitly resolved, or with vertical profiles of temperature and salinity, when insufficient cavity data is available. We present this model as a possible reduced-physics solution to bridge the resolution gap between ocean and ice sheet models. LADDIE can thus be used to force stand-alone ice sheet models with output from Earth System Models, or, ~~after some modification,~~ ~~could function~~ as a dynamical coupler between an ocean and ice sheet model.

~~To test the performance of LADDIE for the whole Antarctic region~~ The aim of this study is threefold. First, we introduce the model LADDIE by describing its physical and numerical basis. Second, we apply it to two the model to two use cases in order to compare the model performance to observations and 3D model simulations. Third, we discuss new melt features at these two use cases that cannot be derived from either observations or (coarser) 3D model simulations. The two use cases are two categorically different ice shelves. The first is the ~~Crosson-Dotson Crosson-Dotson~~ Ice Shelf, representative ~~for of~~ warm ice shelves along West Antarctica. This ice shelf is relatively well studied through in-situ ocean observations (Jenkins et al., 2018) and remote sensing (Gourmelen et al., 2017; Khazendar et al., 2016), giving ample material for ~~validation evaluation~~. The second case study is the ~~Filchner-Ronne Filchner-Ronne~~ Ice Shelf, which is representative ~~for of the large~~ cold ice shelves ~~along most of East around~~ Antarctica. This ice shelf is also relatively well studied through in-situ observations (Nicholls et al., 2009; Hattermann et al., 2021; Bull et al., 2021), remote sensing (Moholdt et al., 2014), ocean modeling (Bull et al., 2021; Naughten et al., 2021), and tidal modeling (~~Padman et al., 2018; Hausmann et al., 2020~~) (Makinson et al., 2011; Padman et al., 2018; Hausmann et al., 2020).

## 2 Methods

To illustrate and validate the performance of the LADDIE model, we base this study on simulations of two ice shelves of opposite character. The first is the Crosson-Dotson Ice Shelf, a relatively small ice shelf in the warm Amundsen region. The second is the Filchner-Ronne Ice Shelf, Antarctica's second-largest ice shelf, residing in the cold Weddell Sea. In this section, we introduce the model LADDIE and the simulations performed for the two use cases Crosson-Dotson and Filchner-Ronne. In Sec. 2.1, we describe the model equations of LADDIE and their numerical implementation. In Sec. 2.2, we describe the external data used to configure, force, and evaluate the model. Finally, in Sec. 2.3, we describe the model setup including the geometry of the Crosson-Dotson and Filchner-Ronne Ice Shelves, the forcing applied for the simulations, and the parameter settings.

### 2.1 Model description

LADDIE is a two-dimensional model, built upon earlier 2D models of the meltwater layer beneath ice shelves (Holland and Feltham, 2006; Hewitt, 2020). The equations are based on the vertically-integrated Navier-Stokes equations, reduced by the Boussinesq approximation and a turbulence closure. In addition, the boundary conditions are partly based on parameterisations as described below. The model explicitly solves for the horizontal fields of layer thickness, 2D velocity, temperature and salinity. LADDIE can be seen as the numerical 2D expansion of the 1D plume model (Jenkins, 1991; Lazeroms et al., 2019), thus resolving the Coriolis deflection and topographic steering of the flow within the meltwater layer.

#### 2.1.1 Governing dynamics

At the heart of the model is a set of five equations for the conservation of the vertically integrated volume, momentum, heat and salt of the meltwater layer (see Fig. 1):

$$\frac{\partial D}{\partial t} + \nabla \cdot (DU) = \dot{m} + \dot{e} \quad (1)$$

$$\frac{\partial DU}{\partial t} + \nabla \cdot (DUU) - fDV = -\frac{gD^2}{2\rho_0} \frac{\partial \Delta \rho_a}{\partial x} + g'_a D \frac{\partial (z_b - D)}{\partial x} - C_{dd,mom} |U|U + \nabla \cdot (A_h D \nabla U) \quad (2)$$

$$\frac{\partial DV}{\partial t} + \nabla \cdot (DUV) + fDU = -\frac{gD^2}{2\rho_0} \frac{\partial \Delta \rho_a}{\partial y} + g'_a D \frac{\partial (z_b - D)}{\partial y} - C_{dd,mom} |U|V + \nabla \cdot (A_h D \nabla V) \quad (3)$$

$$\frac{\partial DT}{\partial t} + \nabla \cdot (DUT) = \dot{e}T_a + \dot{m}T_b - \gamma_T(T - T_b) + \nabla \cdot (K_h D \nabla T) \quad (4)$$

$$\frac{\partial DS}{\partial t} + \nabla \cdot (DUS) = \dot{e}S_a + \nabla \cdot (K_h D \nabla S) \quad (5)$$

Here, the derivation of the pressure gradient terms in these equations is presented for a dense bottom boundary layer by Killworth and Edwards (1999).  $D$  is the layer thickness in m;  $\mathbf{U} = (U, V)$  is the velocity vector along the ice-ocean interface, containing  $U$  and  $V$ , the vertically averaged velocities in  $x$  and  $y$  directions in  $\text{m s}^{-1}$ ;  $T$  and  $S$  are the vertically averaged temperature in  $^\circ\text{C}$  and salinity in psu. Sources and sinks of layer thickness are both melting/freezing at the ice-ocean boundary,  $\dot{m}$ , and entrainment/detrainment at the bottom of the meltwater layer,  $\dot{e}$ . These are fluxes are directed into the meltwater layer.

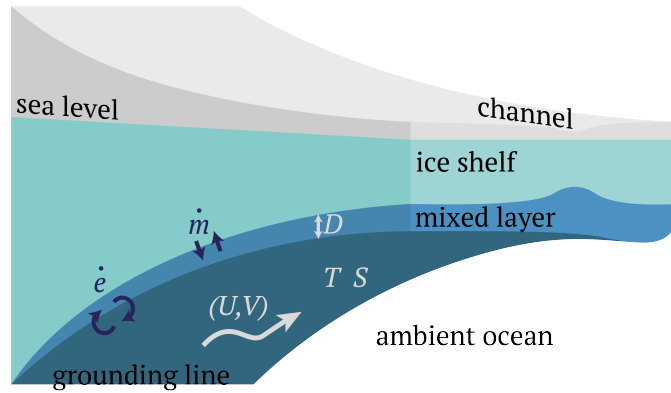


**Figure 1.** Illustration of the LADDIE model. The model solves for five variables describing the meltwater layer beneath the ice shelf, denoted by the white letters. The dark blue letters denote fluxes at the top of the layer ( $\dot{m}$ , melt and freezing) and at the bottom of the layer ( $\dot{e}$ , entrainment and detrainment). The model is forced with geometric boundary conditions (grounding line, ice shelf front, and ice shelf topography) and temperature and salinity of the ambient ocean below the meltwater layer.

so  $\dot{m} > 0$  denotes net melt and  $\dot{e} > 0$  denotes net entrainment. These fluxes are expressed as velocities perpendicular to the model's plane and their parameterisation is described in Sec. 2.1.2.  $A_h$  is the horizontal viscosity,  $K_h$  the horizontal diffusivity, and  $\gamma_T$  is the turbulent exchange velocity of heat in the ice–ocean boundary layer; the latter is parameterised as described in Sec. 2.1.2. Note that we assume ice to be of salinity 0, hence no melt term appears in the salt budget.

The subscript  $a$  refers to variables in the motionless ‘ambient’ ocean below the layer, and to variables at the interface between the layer and the ambient water below.  $g'_a$  is the reduced gravity, describing the effective gravitational acceleration due to density differences in seawater:

$$g'_a = g \frac{\Delta\rho_a}{\rho_0} \quad (6)$$

$\Delta\rho_a$  is the density difference between the layer and the ambient water below the layer. We assume a linear equation of state:

$$\Delta\rho_a = \rho_0(-\alpha(T_a - T) + \beta(S_a - S)) \quad (7)$$

The ambient temperature  $T_a$  and salinity  $S_a$  function as forcing fields in the model. These depth-dependent variables are derived from external input, as described in Sec. 2.3.2. In this equation,  $\alpha$  is the thermal expansion coefficient and  $\beta$  the haline contraction coefficient.

The subscript  $b$  refers to the ice shelf base, and variables at the ice–ocean interface.  $z_b$  is the depth of the ice shelf draft in meters below sea level (note:  $z_b < 0$ );  $T_b$  is the temperature at the ice–ocean boundary.

The remaining fixed parameters are the Coriolis frequency  $f$ , the gravitational acceleration  $g$ , the reference density  $\rho_0$ , and the drag coefficient  $C_a$  momentum drag coefficient  $C_{d,mom}$ . All fixed parameter values are given in Table 1. Finally, a number of parameters are used as tuning parameters or adapted to assure numerical stability under different configurations. These parameter values are listed in Table 2.

## 2.1.2 Boundary conditions

The vertical exchange of volume, heat and salt is governed by freezing or melt ( $\dot{m}$  at the top boundary) and entrainment or detrainment ( $\dot{e}$  at the bottom boundary). Here, we describe LADDIE's parameterisations governing  $\dot{m}$  and  $\dot{e}$ , as well as its lateral boundary conditions.

180 The top boundary condition  $\dot{m}$  is computed by solving the widely-adopted ‘~~three equations’-equation’~~ formulation for melt and freezing, comprising the conservation of heat and salt as well as an equation ~~of state. The latter constrains~~ ~~constraining~~ the ice–ocean boundary to remain at the freezing point  $T_f$  (Holland and Jenkins, 1999; Jenkins et al., 2010):

$$C_p \gamma_T (T - T_b) = \dot{m} L + \dot{m} C_I (T_b - T_i) \quad (8)$$

$$\gamma_S (S - S_b) = \dot{m} S_b \quad (9)$$

185 
$$T_b = \lambda_1 S_b + \lambda_2 + \lambda_3 z_b \quad (10)$$

Here,  $T_i$  is the temperature of the ice shelf interior, which functions as a forcing parameter.  ~~$C_p$  is the heat capacity of seawater.~~  $C_I$  is the heat capacity of ice,  $L$  is the latent heat of fusion for ice, and  $T_b$  and  $S_b$  are the temperature and salinity at the ice–ocean interface. ~~The three parameters  $\lambda_n$  specify the pressure melting point.~~

In the above parameterisation for  $\dot{m}$ ,  $\gamma_T$  and  $\gamma_S$  are the turbulent exchange velocities of heat and salt in  $\text{m s}^{-1}$ , which we  
190 parameterise following Jenkins (1991):

$$\gamma_T = \frac{U_*}{2.12 \log(U_* D / \nu_0) + 12.5 Pr^{2/3} - 8.68} \quad (11)$$

$$\gamma_S = \frac{U_*}{2.12 \log(U_* D / \nu_0) + 12.5 Sc^{2/3} - 8.68} \quad (12)$$

Here,  $\nu_0$  is the ~~molecular kinematic~~ viscosity,  ~~$Pr$  is the Prandtl number,~~ and  ~~$Sc$  is the Schmidt number~~ ~~are the molecular Prandtl and Schmidt numbers of seawater respectively.~~

195 In the latter equations,  $U_*$  is the friction velocity, defined as in Jenkins et al. (2010):

$$U_* = \sqrt{C_{d,top} (U^2 + V^2 + U_{tide}^2)} \quad (13)$$

Here,  $U_{tide}$  is ~~the mean-a time-mean~~ tidal velocity in  $\text{m s}^{-1}$ , which functions as a forcing parameter for the model.  $C_{d,top}$  is a ~~specific~~-drag coefficient applied ~~only~~ to the friction velocity used in the ‘~~three equations’-melting formulation~~ (Eq. 8). Note that, following Asay-Davis et al. (2016), we introduce this separate drag coefficient alongside  $C_d C_{d,mom}$ , which is used in the  
200 momentum equations (Eq. 4).  ~~$C_{d,top}$  is commonly taken to be lower than  $C_d$ . This difference is imposed 2, 3). This separation into two drag coefficients is sometimes applied in 3D ocean models~~ to correct for ~~the presence of stratification which is neglected in the ‘three equations’, as discussed by (e.g., Holland and Feltham, 2006).~~ ~~neglected processes, such as stratification, in the melting formulation (see discussion by, e.g., Holland and Feltham (2006)).~~ In the current study,  $C_d C_{d,mom}$  is fixed (Table 1), whereas  $C_{d,top}$  is treated as a tuning parameter (Sec. 2.3.3).

205 The bottom boundary conditions govern the entrainment  $\dot{e}$  of ambient water into the ~~upper-ocean-meltwater~~ layer. This entrainment has been described by a wide variety of different parameterisations (Jenkins, 1991; Holland and Feltham, 2006).

In each of these parameterisations, entrainment is expressed as a function of the turbulent velocity in the meltwater layer. However, under conditions of weak turbulence, detrainment may occur. This process reverses the transport between the upper layer and the ambient waters, thinning the layer. Detrainment is an important process to prevent the layer thickness from growing indefinitely. We therefore ~~adopt~~ follow Gladish et al. (2012) in adopting the parameterisation from Gaspar (1988) describing entrainment and detrainment ~~of dense overflows from an ocean surface mixed layer:~~

$$\frac{D}{2} g'_b \dot{m} + \frac{D}{2} g'_a \dot{e} = \mu U_*^3. \quad (14)$$

Here, ~~negative~~  $\mu$  is a nondimensional parameter. Negative values for  $\dot{e}$  represent detrainment fluxes. This parameterisation ~~is based on the balance in~~ describes the balance between the source of turbulent kinetic energy (TKE) ~~within the meltwater layer. The source of TKE~~ from frictional stress at the ice base ( $U_*$  term) ~~is balanced by and~~ the buoyancy sink of TKE from melting and entrainment. In this expression, the dissipation of TKE is assumed to occur as a fixed fraction of the rate of TKE production, and is therefore embedded in the parameter  $\mu$ . This parameterisation was previously used in the 3D ocean model MICOM (Holland and Jenkins, 2001) and in an earlier example of the layer model (Gladish et al., 2012). Note that the same value for  $U_*$  is used, based on  $C_{d,top}$ , as in Eq. 8. Whether  ~~$C_d$~~   $C_{d,mem}$  or  $C_{d,top}$  is the more appropriate choice for Eq. 14 can be debated. However, as  $\mu$  is an arbitrary constant that can be tuned accordingly, both options are equivalent.

The lateral boundary conditions in LADDIE are split between closed and open boundaries. The closed boundaries apply at the grounding line, where the ice shelf cavity meets the grounded ice. Here, zero gradients are prescribed in  $D$ ,  $T$ , and  $S$ . In addition, a partial slip condition is prescribed for  $U$  and  $V$ , similar to that included in the NEMO model ~~(?)~~ This (Madec et al., 2019). To optimise the flexibility of the model, this partial slip condition ~~is a weighted average describes a spectrum~~ between free slip and no slip; ~~the weighting is,~~ rather than only allowing the latter two options. In the partial slip condition, lateral friction is scaled down compared to no slip. The slip condition is governed by a parameter ranging between 0 (free slip) and 2 (no slip). ~~This parameter can be freely chosen.~~ In the current study, we apply a value of 1, though a sensitivity analysis revealed that the parameter choice has a weak impact on the simulated basal melt patterns.

At the open boundaries, where the cavity meets the open ocean below the ice-shelf front, zero gradients are applied to all variables  $D$ ,  $T$ ,  $S$ ,  $U$ , and  $V$ . These conditions allow the model to converge to a ~~solution with a~~ steady solution where the net outflow from the cavity into the deep ocean ~~,balancing~~ balances the integrated volume, heat, and salt fluxes due to entrainment and melt.

### 2.1.3 Numerical implementation

The horizontal grid is discretised ~~in as~~ a staggered Arakawa-C grid, in which velocities  $U$  and  $V$  are solved at the grid cell edges, and the other variables  $D$ ,  $T$ , and  $S$  are solved at grid centers. The advection of volume, heat, and salt is applied using an upstream biased advection scheme. After trial and error testing various options, this scheme was found to be most stable.

The numerical integration in time is performed using a leapfrog scheme with Robert-Asselin filter, similar to that in the NEMO model ~~(?)~~ (Madec et al., 2019). This filter functions as a diffusion in time ~~,described and is set~~ by parameter  $\nu$  between 0 and 1. In the NEMO model description,  $\nu = 0.1$  is presented as a reference value. Using this same value in LADDIE was

**Table 1.** Model parameters. PMP = pressure melting point.

parameter	meaning	value	unit
$f$	Coriolis frequency	$-1.37 \times 10^{-4}$	$s^{-1}$
$g$	gravitational acceleration	9.81	$m s^{-2}$
$\rho_0$	reference seawater density	1028	$kg m^{-3}$
$C_d C_{d,moon}$	<del>momentum</del> drag coefficient	$2.5 \times 10^{-3}$	-
$\alpha$	thermal expansion <del>coefficient</del>	$3.733 \times 10^{-5}$	$^{\circ}C^{-1}$
$\beta$	<del>saline contraction</del> <del>haline contraction coefficient</del>	$7.843 \times 10^{-4}$	$psu^{-1}$
$C_p$	heat capacity of seawater	3974	$J kg^{-1} ^{\circ}C^{-1}$
$L$	latent heat of fusion	$3.34 \times 10^5$	$J kg^{-1}$
$C_I$	heat capacity of ice	2009	$J kg^{-1} ^{\circ}C^{-1}$
$\lambda_1$	PMP salinity parameter	$-5.73 \times 10^{-2}$	$^{\circ}C psu^{-1}$
$\lambda_2$	PMP offset parameter	$8.32 \times 10^{-2}$	$^{\circ}C$
$\lambda_3$	PMP depth parameter	$7.61 \times 10^{-4}$	$^{\circ}C m^{-1}$
$\nu_0$	<del>molecular</del> <del>kinematic</del> viscosity	$1.95 \times 10^{-6}$	$m^2 s^{-1}$
$Pr$	<del>molecular</del> Prandtl number	13.8	-
$Sc$	<del>molecular</del> Schmidt number	2432	-
$\mu$	detrainment parameter	0.5	-

240 found to require a relatively short time step to maintain numerical stability. We found that a value of  $\nu = 0.8$  produces identical steady state solutions ~~and allows~~ ~~whilst allowing~~ for a longer time step. Because in this study, we only focus on steady state solutions, we chose to keep the value of  $\nu = 0.8$ . However, the choice of  $\nu$  does affect the transient state, and future applications of the model should reassess this parameter choice.

A general issue in 2D models, ~~similar to isopycnal 3D models~~, is that the model requires a finite thickness  $D$  in order to remain numerically stable. In some regions, set by the topography of the ice shelf draft  $z_b$ , the velocity field tends to be divergent, particularly near grounding lines. In some cases, the entrainment flux  $\dot{e}$  is insufficient to compensate for this divergent flow, leading to a gradual thinning of the model layer. This issue was discussed in detail by Gladish et al. (2012), who proposed the solution of imposing a minimum layer thickness  $D_{min}$ . One can interpret this solution as being equivalent to the fixed upper grid thickness in 3D ocean models. Here, we adopt this solution by increasing the local entrainment flux as required when the thickness would otherwise drop below  $D_{min}$ . We treat the parameter  $D_{min}$  as a tuning parameter, as described in Sec. 2.3.3.

## 2.2 External data

For the model simulations and ~~validation, we have used~~ ~~evaluation, we use~~ a number of data sets from external sources. Here, we briefly discuss their source, their underlying methodology, and some of their limitations.

## 255 2.2.1 Geometry

The realistic simulation of ice shelf basal melt rates with LADDIE strongly depends on the applied geometry. Here, we have taken the geometry from the Bedmachine v2 data set (Morlighem et al., 2020). This data set combines remote sensing products of the Antarctic ice surface elevation and velocity into a consistent map of ice thickness and bed topography below grounded ice. For the floating ice shelves, the ice shelf thickness is based on the assumption of hydrostatic equilibrium, a modeled firn  
260 layer, and an additional firn-depth correction. Within 3 ~~kilometers~~ kilometres from the grounding line, ~~smoothing of the~~ the ~~authors have smoothed the~~ ice shelf thickness ~~is applied~~ to ensure continuity.

Whilst providing a detailed, high resolution geometry, the Bedmachine data set contains some limitations which are relevant to our study. The smoothing within 3 km from the grounding line removes detailed topographic features in this region. In addition, the grounding line is static, which prevents the modeling of basal melt nearby retreating grounding lines. At small  
265 scales, the assumption of hydrostatic equilibrium may also be violated by a significant internal stress, obscuring the topography of basal channels. Finally, the data set provides a snapshot of the highly dynamic ice shelf front and shear margins. This allows LADDIE to simulate instantaneous basal melt rates, but ~~prevents it from simulating time-mean basal melt rates over a~~ these ~~melt rates may not be representative of a~~ multi-year ~~period. The above limitations hamper the direct validation of modeled basal melt rates to observations. As the aim for LADDIE is to simulate basal melt patterns consistent with the provided topography, we will not purely validate LADDIE to observations. In addition, we will qualitatively infer reasonable basal melt patterns for the given topography. For example, the presence of a basal channel in the applied geometry should impact the simulated flow — and possibly the basal melt rate — by LADDIE, regardless of whether this channel is a realistic feature or an artefact of the topography. In other words, an unrealistic topographic feature should induce an unrealistic yet physically consistent basal melt pattern by LADDIE.~~ period in some regions.

## 275 2.2.2 Observations

~~To quantitatively validate~~ To quantitatively evaluate LADDIE, we compare the simulated basal melt patterns to basal melt rates derived from remote sensing products. For simplicity, we refer to these basal melt rates as ‘observations’, while stressing that they are highly uncertain and based on a range of assumptions. Therefore, these observations should not be interpreted as a ground truth.

280 For the ~~Crosson-Dotson~~ Crosson-Dotson Ice Shelf, we ~~validate LADDIE to observations from Gourmelen et al. (2017); Goldberg et al. (2019)~~ evaluate LADDIE against observations from Gourmelen et al. (2017) and Goldberg et al. (2019). These basal melt rates are derived from CryoSat-2 radar altimetry over the period 2010-2016. Changes in surface elevation are processed using a Lagrangian analysis based on observed surface ice velocities. ~~These changes are then combined~~ Together with modeled surface mass balance and the assumption of hydrostatic equilibrium ~~to provide~~, these observations are used to construct a mass balance, from  
285 which basal melt rates are derived.

Besides uncertainties in the underlying observations, the assumption of hydrostatic equilibrium induces a large uncertainty near grounding lines. This uncertainty was assessed by Milillo et al. (2022) for the ~~Crosson-Dotson~~ Crosson-Dotson Ice

Shelf and was found to be small in the Kohler grounding zone, yet large in the Smith grounding zone. Another issue with observations in the grounding zone is the timing and the relatively long period over which basal melt rates are assessed. The Kohler, Smith, and Pope grounding lines are known to have retreated at a high rate over the last decade (Scheuchl et al., 2016; Milillo et al., 2022). This makes average basal melt rates over a multi-year period in this region (e.g., [Gourmelen et al., 2017](#)) less representative of instantaneous basal melt rates as simulated by LADDIE.

For the ~~Filehner-Ronne~~-[Filchner-Ronne](#) Ice Shelf, we use the Antarctic-wide observations from Adusumilli et al. (2020). The underlying methodology is similar to that of Gourmelen et al. (2017); it is based on a combination of CryoSat-2 altimetry, satellite-derived surface ice velocities, and modeled firn layer. The firn density model used in this study is of a coarse resolution (12.5 km) compared to the grid size of the final product (500 m). In addition, no recalibration based on local observations is applied as in Gourmelen et al. (2017). Together, these differences lead to a poorer spatial detail in the ‘observed’ basal melt fields. However, comparison to other remote sensing estimates (Rignot et al., 2013; Moholdt et al., 2014) gives confidence in the assessed large-scale pattern of basal melting and freezing.

### 300 2.2.3 3D model reference

In this study, we introduce LADDIE as a new model to simulate high-resolution spatial basal melt patterns. To test its added value compared to 3D numerical ocean models, we compare the simulated basal melt fields for ~~Crosson-Dotson and Filehner-Ronne~~-[Crosson-Dotson and Filchner-Ronne](#) to regional 3D model output. [This comparison output is chosen for the quality of the basal melt patterns, its availability, and its representation of a steady state.](#)

For the ~~Crosson-Dotson~~-[Crosson-Dotson](#) Ice Shelf, we compare basal melt from LADDIE to that simulated by a regional setup of MITgcm of the Amundsen region with resolved ice shelf cavities (Naughten et al., 2022). The ocean/sea-ice model is configured with a horizontal grid size ranging from 5.2 km offshore to 2.8 km at its ~~shouthernmost~~-[southernmost](#) point. The geometry is based on the BedMachine v2 geometry and the model is forced with ERA5 atmospheric reanalysis (Hersbach et al., 2020). The model was extensively tuned to reproduce observations in the region. In particular, the ocean conditions and their interannual variability in front of Dotson and Pine Island ~~Ice Shelves~~-[ice shelves](#) were tuned to match observations by varying sea-ice parameters, and then the melt rates for these ice shelves were tuned to match observations by selecting melting parameter values that best fit the entire region (Naughten et al., 2022). For an optimal comparison to the observations from Rignot et al. (2013), we extract and average the period 2003–2008 from the MITgcm simulation.

For the ~~Filehner-Ronne~~-[Filchner-Ronne](#) Ice Shelf, we compare the basal melt rates from LADDIE to regional simulations using NEMO (Hausmann et al., 2020). NEMO, similar to MITgcm, is an advanced ocean/sea-ice model, with explicitly resolved cavities. The regional simulation of the Weddell Sea was configured at a horizontal resolution varying between 4.5 km offshore to 1.5 km at the southernmost point. The model was forced with atmospheric climatology from CORE-2 (Large and Yeager, 2009), and tidal conditions at the open boundaries from FES2012 (Carrere et al., 2013). The model was specifically designed to simulate tides in the ~~Filehner-Ronne~~-[Filchner-Ronne](#) cavity and their impact on basal melt and freezing.

320 Both 3D ocean/sea-ice models are configured using a fixed vertical grid. The vertical grid cell thickness below the ice shelves ranges between 10 and 50 m for MITgcm and between 10 and 150 m for NEMO. In both models, basal melt and freezing is parameterised using a similar ‘three-equation’ formulation as used in LADDIE (Eq. 8).

## 2.3 Model setup

325 In this section, we describe the model setup for the simulations of the ~~Crosson-Dotson and Filchner-Ronne~~ Crosson-Dotson and Filchner-Ronne Ice shelves (Fig. 2).

### 2.3.1 Geometry

~~The geometry of the model domain is given by the topography of the ice shelf draft  $z_b$  and the classification of the lateral boundaries. We base our geometry on the BedMachine v2 data set (Morlighem et al., 2020), which provides an ice shelf draft topography at a  $500 \times 500$  m<sup>2</sup> grid for the entire Antarctic ice sheet. The classification of the lateral boundaries is~~  
330 ~~based on the embedded mask of grounded ice, floating ice, and open ocean; from this mask, lateral boundaries are separated into open boundaries (the ice shelf front) and closed boundaries (the grounding line).~~ Due to its relatively small size, the ~~Crosson-Dotson~~ Crosson-Dotson Ice Shelf can be configured on the original resolution of  $500 \times 500$  m<sup>2</sup> of the BedMachine v2 data set (Morlighem et al., 2020) without a problem. Note that previous studies have smoothed the ice shelf topography, in part to ensure numerical stability (e.g., Holland et al., 2007), which is a common practice in ice-ocean modeling  
335 ~~(Asay-Davis et al., 2016)~~ (e.g., Asay-Davis et al., 2016). In order to resolve ~~kilometer-scale~~ kilometre-scale basal melt features, LADDIE is configured such that it can deal with unmodified ice shelf topography.

For the ~~Filchner-Ronne~~ Filchner-Ronne Ice Shelf, simulations at  $500 \times 500$  m<sup>2</sup> are computationally demanding, as the LADDIE model is not yet coded in parallel. Hence, this ice shelf is configured at a  $1000 \times 1000$  m<sup>2</sup> resolution by averaging the topography of  $2 \times 2$  neighbouring grid cells.

### 340 2.3.2 Forcing

The LADDIE model ~~is forced by four variables~~ takes four variables as external forcing: the ambient temperature and salinity,  $T_a$  and  $S_a$ ; the ice shelf temperature  $T_i$ ; and the tidal velocity  $U_{tide}$ . In this study, we ~~choose to focus mainly on apply~~ idealised forcing fields. ~~This choice allows for easier,~~ allowing for a straightforward interpretation of the results and ~~for a cleaner a clean~~ assessment of the ~~impact of geometry on the resultant basal melt fields~~ geometric impact on basal melt patterns.  
345 To test the sensitivity of the basal melt patterns to ~~the applied this choice of idealised~~ forcing, we include a comparison for ~~Crosson-Dotson~~ Crosson-Dotson to a more realistic 3D forcing (App. A).

For both ~~Crosson-Dotson and Filchner-Ronne~~ Crosson-Dotson and Filchner-Ronne Ice Shelves, we apply uniform fields of  $T_i$  and  $U_{tide}$ . The values are listed in Table 2. We note that  $U_{tide}$  has a large impact on the heat transfer toward the ice shelf base. In particular for ~~Filchner-Ronne, significant improvements may be possible when changing  $U_{tide}$  to a spatially variable~~ field (Padman et al., 2018; Hausmann et al., 2020). ~~Filchner-Ronne, an accurate spatially heterogeneous tidal forcing may~~

350

significantly improve the accuracy of basal melt patterns (Hausmann et al., 2020). However, we note that the tidal fields used most commonly to force 3D ocean models contain substantial errors in several Filchner–Ronne grounding zones (Padman et al., 2018). As we discuss in Sec. 3.2.2, this can lead to erroneous basal melt patterns. A detailed assessment of the accuracy and impact of tidal forcing is beyond the scope of this study, and we therefore proceed with uniform tidal forcing.

355 For  $T_a$  and  $S_a$ , the main results in this paper are based on idealised vertical profiles of temperature and salinity. ~~This is done for two~~ We choose this approach for a number of reasons. First, as described above, an idealised forcing eases the interpretation of the ~~impact of geometry~~ geometric impact on the simulated basal melt patterns. Second, 1D vertical profiles resemble the output of Earth System Models without resolved cavities; we anticipate that forcing with such ESM output ~~is will be~~ a main application of the model. ~~Below, we describe the prescribed temperature and salinity fields used as forcing. From these steady fields, at each model time step, temperatures and salinities at each grid cell are extracted at the depth of the layer base,  $z_b = D$ . These temperatures and salinities form the horizontal 2D fields of  $T_a$  and  $S_a$  at the layer base. For the main simulations of the Crosson-Dotson Ice Shelf, we create vertical~~ Third, observations in front of the ice shelves are available (Nicholls et al., 2009; Jenkins et al., 2018), yet these are subject to a summer bias and substantial interannual variability; whether these observations are representative for the long-term ocean state is unclear. Based on this reasoning, we

360 ~~choose to present model results based on simulations with idealised 1D profiles mimicking the observed profiles in front of the Dotson Ice Shelf (Jenkins et al., 2018) forcing.~~

The forcing profiles for both ice shelves are shown in Fig. 2. The profiles for Crosson–Dotson mimic an average state from the observations by Jenkins et al. (2018). Temperature is described by a tangent hyperbolic function, ranging from  $-1.7^\circ\text{C}$  at the surface to  $+0.4^\circ\text{C}$  at 1200 m depth (Fig. 2e). The thermocline is centered at 500 m depth with a scale factor of 250 m. This

370 temperature profile describes the observed two-layer stratification in front of the ice shelf. Salinity increases from 34 psu at the surface to 34.5 psu at 1200 m depth. The profile is derived from a prescribed density profile, which is quadratic with depth; this density profile mimics the observed ~~strongest stratification~~ stratification maximum near the surface.

~~To test the sensitivity of the simulated Crosson-Dotson basal melt patterns to the applied forcing, we also include a simulation with 3D forcing (see App. A). As it is considered the most realistic option, this 3D forcing is also used for the model tuning (see~~

375 ~~App. B). The 3D fields of temperature and salinity are derived from the simulations with MITgem (see Sec. 2.2.3) averaged over the period 2003–2008. This period aligns with the observation period of Rignot et al. (2013), which is used to tune LADDIE. From the 3D model output within the cavity, the upper two grid cells below the ice shelf are removed, as these represent the meltwater layer rather than the ambient waters. To extract ambient temperatures and salinities throughout the cavity, the remaining 3D fields are regridded onto the LADDIE grid, extrapolated vertically to the ice shelf base, and horizontally into~~

380 ~~missing grid cells. Finally, to ensure smooth and continuous profiles of temperature and salinity, a vertical smoothing is applied with a window of 10 meters. For the Filchner–Ronne~~ For the Filchner–Ronne Ice Shelf, we apply idealised profiles of temperature and salinity approximating the average conditions within this cold cavity. These profiles are similar to those applied to the ~~Filchner–Ronne~~ Filchner–Ronne simulations by Holland et al. (2007). Temperature decreases linearly from freezing point at the surface to  $-2.3^\circ\text{C}$  at 2000 m depth. Salinity increases linearly from 34.5 psu at the surface to 34.8 psu at 2000 m depth

385 (Fig. 2d)–f).

From these vertical profiles, at each model time step, temperatures and salinities at each grid cell are extracted at the depth of the layer base,  $z_b - D$ . These temperatures and salinities form the horizontal 2D fields of  $T_a$  and  $S_a$  at the layer base.

In the appendix, we present an additional use case for Crosson–Dotson. Here, the model is forced with 3D cavity fields from simulations with MITgcm (see Sec. 2.2.3). We describe this more advanced forcing, and its impact on basal melt patterns, in App. A. In addition, this 3D forcing is used to tune the model, as described in detail in App. B.

### 2.3.3 Parameter settings

With the geometry and forcing described above, the model setup is completed by a number of parameter choices. A number of parameter values remain unspecified in order to adapt them to different simulations. These are the time step  $\Delta t$ , the horizontal viscosity  $A_h$  and the horizontal diffusivity  $K_h$ ; each of these affects the numerical stability of the model and depend on the chosen resolution. Finally, two parameters are considered tuning parameters:  $C_{d,top}$  and  $D_{min}$ .

Based on trial and error, we have determined values of  $A_h$  of 100, 50, and 25  $\text{m}^2 \text{s}^{-1}$  to be suitable for grid resolutions of 2000, 1000, and 500 m, respectively. Further sensitivity runs indicated that the choice of  $K_h$  has only a small effect on the resultant basal melt rates; for convenience, we take  $K_h$  equal to  $A_h$ . Finally, values for the time step  $\Delta t$  are determined per configuration in order to maximise the time step while ensuring numerical stability. The values for the main simulations of the ~~Crosson–Dotson and Filchner–Ronne~~ Crosson–Dotson and Filchner–Ronne Ice Shelves are shown in Table 2. Note that the values of  $A_h$  and  $K_h$  exceed those by Asay–Davis et al. (2016) for reasons of numerical stability; lower values can be used when sufficiently reducing the time step  $\Delta t$  and/or smoothing the topography.

We have chosen to treat the remaining two parameters as tuning parameters, namely the drag coefficient used in the equation for the friction velocity  $C_{d,top}$  and the minimum layer thickness  $D_{min}$ .  $C_{d,top}$  is commonly used for tuning the basal melt parameterisation in ocean models (Holland and Feltham, 2006); values in the literature vary between  $1.0 \times 10^{-3}$  (Jourdain et al., 2017; Mathiot et al., 2017) and  $9.7 \times 10^{-3}$  (Jenkins et al., 2010).  $D_{min}$  is treated as a tuning parameter, as its impact on basal melt rates is found to be relatively large. Here, we have considered values between 2 and 8 meters.

The model is tuned to a number of ~~observational-based~~ observation-based indicators for the ~~Crosson–Dotson~~ Crosson–Dotson Ice Shelf. The resultant tuning parameters are applied to the ~~Filchner–Ronne~~ Filchner–Ronne Ice Shelf in order to test whether the tuning is valid in both cold and warm environments. Five diagnostics are derived from simulations with 3D forcing: ice-shelf average melt, melt in the Kohler grounding zone, melt along the wide Dotson Channel and along its center line, and the total overturning circulation. These diagnostics are compared to a number of remote sensing and in-situ observational sources. For horizontal grid sizes of  $500 \times 500$ ,  $1000 \times 1000$  and  $2000 \times 2000 \text{ m}^2$ , values of  $D_{min}$  and  $C_{d,top}$  are determined such that each of the five diagnostics fall within the assessed uncertainty ranges. The complete tuning procedure is described in Appendix B, and the values used in our simulations are shown in Table 2.

We note that the model is tuned to Crosson–Dotson, and partly evaluated on the same ice shelf. However, merely two tuning parameters are used for five tuning targets and an evaluation of the complete melt pattern. Therefore, we consider this tuning procedure to be valid. As additional proof of the validity of this tuning procedure, we include a simulation for the Pine Island Ice Shelf, another small ice shelf in the warm Amundsen Sea region, in Appendix C.

**Table 2.** Simulation-specific parameter values applied the ~~Crosson-Dotson~~ Crosson-Dotson and the ~~Filchner-Ronne~~ Filchner-Ronne Ice Shelves.

parameter	meaning	<del>Crosson-Dotson</del> <u>Crosson-Dotson</u>	<del>Filchner-Ronne</del> <u>Filchner-Ronne</u>	units
$\Delta x$	resolution	500	1000	m
$T_i$	ice temperature	-25	-25	°C
$U_{tide}$	tidal velocity	0.01	0.1	$\text{m s}^{-1}$
$A_h$	hor. viscosity	25	50	$\text{m}^2 \text{s}^{-1}$
$K_h$	hor. diffusivity	25	50	$\text{m}^2 \text{s}^{-1}$
$C_{d,top}$	<del>exchange-top drag</del> coefficient	$1.1 \times 10^{-3}$	$1.1 \times 10^{-3}$	
$D_{min}$	minimum thickness	2.8	4.4	m
$\Delta t$	time step	120	240	s
	equilibration time	30	720	model days
	computation time	0.5	60	CPU hours

#### 420 2.3.4 Experimental design

Using the configuration and parameter settings above, the equations are integrated forward in time. The layer is initialised at rest,  $U = V = 0$ , and the initial layer is uniformly 10 m thick. For temperature and salinity,  $T$  and  $S$ , initial values are taken  $0.1^\circ\text{C}$  and  $0.1$  psu below the ambient values  $T_a$  and  $S_a$  respectively. This small initial difference in salinity ensures a stable stratification.

425 The current model setup is designed to simulate basal melt rates under steady state conditions, with a fixed geometry and fixed ambient conditions. The results presented in this study are thus steady state basal melt rates. For the ~~Crosson-Dotson~~ Crosson-Dotson Ice Shelf, basal melt rates are averaged over the last 5 model days; for ~~Filchner-Ronne~~ Filchner-Ronne over the last 10 model days. The equilibration time, as well as the computation time required for a full spin up, is listed in Table 2.

### 3 Results

430 In this section, we present the steady-state basal melt patterns simulated by LADDIE for the ~~Crosson-Dotson and the Filchner-Ronne~~ Crosson-Dotson and the Filchner-Ronne Ice Shelves consecutively. For each ice shelf, we ~~begin with discussing the large-scale ice shelf-wide pattern of melt and freezing. We then continue to discuss detailed spatial melt patterns in specific regions of both ice shelves. The simulated melt patterns are compared to~~ divide the results into three parts. The first is a model evaluation compared to available observations (Sec. 2.2.2). The second is a comparison to 3D ocean model simulations (Sec. 2.2.3). The  
 435 third and final part is a description and assessment of novel melt patterns that are simulated by LADDIE, but not visible in either the observations and or the relatively coarse 3D model output. ~~For each melt feature, we assess the reliability of observations, the accuracy of LADDIE and the 3D model, and the implications for the stability of the ice shelves.~~ ocean models.

### 3.1 Crosson-Dotson

### 3.1 Crosson-Dotson

#### 440 3.1.1 Large-scale patterns

In this section, we describe spatial melt patterns of the Crosson-Dotson Ice Shelf (Fig. 3).

~~Across the Crosson-Dotson Ice Shelf, the highest melt rates are found in the regions~~

#### 3.1.1 Model evaluation

445 Across the Crosson-Dotson Ice shelf, remote sensing observations reveal a contrast between high melt rates in deep regions and low melt rates in shallow regions (Fig. 3b). The high melt rates are largely confined to the region where the ice shelf extends below approximately ~~450 meters (Fig. ??b). This corresponds with the approximate~~ 500 m depth. This depth marks the depth of the thermocline , ~~separating deep warm water from cold shallow water (Jenkins et al., 2018). These highest melt rates can thus, to first order, be explained by the local thermal forcing, which is the~~ (see Fig. 2c), below which the ice shelf is in direct contact with Circumpolar Deep Water (Jenkins et al., 2018). This relatively warm water mass induces a large temperature difference  
450 between  ~~cavity waters the ocean water~~ and the freezing temperature point at the ice shelf base ~~(e.g. Favier et al., 2019).~~ ; this temperature difference is defined as the thermal forcing. To first order, it is this strong thermal forcing that explains the high melt rates in the deep ice shelf regions (e.g. Favier et al., 2019).

In the regions of the ice shelf shallower than ~~450 meters~~ the thermocline, a weak thermal forcing induces relatively low basal melt rates (Fig. ~~??3~~b). ~~Even though~~ The remote sensing observations even indicate basal freezing in some shallow  
455 regions ~~appear to show basal freezing; however~~, this is an artefact of the calculation procedure and is considered unrealistic by Goldberg et al. (2019). Overall, the contrast between high melt in the deeper regions and low melt in the shallow regions is well-simulated by ~~both the 3D model MITgem (Fig. ??e) and by~~ LADDIE (Fig. ~~??3~~d).

This large-scale ~~pattern~~ contrast between the deep and shallow regions is violated by one major feature, the Dotson Channel (DC). ~~This channel~~ Whereas this channel resides in the shallow region of the ice shelf, it contains relatively high melt rates.  
460 The Dotson Channel is approximately 5 km wide, is clearly visible in the ice shelf topography (Fig. 3a) and extends from the deep parts of the ice shelf to the shallow ice-shelf front (Gourmelen et al., 2017). ~~Such channels~~ Channels like the Dotson Channel arise due to meltwater plumes which advect relatively warm water from the deep ice shelf regions to the shallow regions (Payne et al., 2007). The accurate modeling of such melt channels therefore requires the explicit simulation of the flow below the ice shelf. As a consequence, ~~these~~ melt channels cannot easily be simulated using models of fewer than ~~2 dimensions~~  
465 two dimensions (e.g., Burgard et al., 2022). The regional melt enhancement in the DC, 1.2 times the ice shelf-average basal melt rate, was part of the tuning procedure in this study (Fig. B). We found that this melt enhancement is relatively insensitive to variations in the tuning parameters. Hence, we conclude that the Dotson Channel is robustly and realistically simulated by LADDIE. Both MITgem and LADDIE reproduce this feature

The evaluation of the LADDIE model is continued by a closer look at the detailed melt pattern across the Dotson Channel. An enlargement of part of the Dotson Channel is shown in Fig. 3e-h. One remarkable feature revealed by the remote sensing observations is the misalignment between the centerline of the topographic channel (Fig. 3e, d) and the centerline of the observed melt peak (Fig. 3f). This misalignment is visualised more clearly in three cross-sections across the Dotson Channel in Fig. 4. Across all three sections, the observed melt peak (orange curves) aligns to the left (west) of the channel's topographic centerline (black vertical lines). This westward amplification of melt rates occurs due to the Coriolis deflection of the northward flowing melt plume, which is directed toward the left in the Southern Hemisphere. These remote sensing observations of Coriolis-enhanced melt by Gourmelen et al. (2017) are supported by observations of basal melt of the Pine Island Ice Shelf (Dutrieux et al., 2013). The asymmetry in melt rates within the Dotson Channel favours a channel geometry that is directed to the left of the ice shelf flow direction (Dutrieux et al., 2013) and can potentially induce a westward migration of the channel due to ice-ocean interactions (Gladish et al., 2012; Sergienko, 2013). The observed misalignment between the topographic channel and the melt peak is accurately reproduced by LADDIE (light-blue curves). This agreement indicates that both the flow of the melt plume and the Coriolis deflection thereof are realistically simulated by LADDIE.

### 3.1.2 Kohler-grounding-zone

~~To discuss the more detailed melt patterns, we zoom in on several key regions. The first of these is the~~

As a final region to evaluate the LADDIE performance of the Crosson-Dotson melt pattern, we look more closely at the Kohler grounding zone (Fig. 3i-l). This is the only deep grounding zone of this ice shelf where valid observations from remote sensing are available. The average melt rates in the grounding zone, derived from remote sensing, are approximately  $25 \text{ m yr}^{-1}$  (Fig. 3j, Gourmelen et al. (2017)). These rates agree well with the average melt rates of  $20 \text{ m yr}^{-1}$  from airborne surveys over the same period (Khazendar et al., 2016). These melt rates are approximately 3–4 times higher than the average melt rates over the whole Crosson-Dotson Ice Shelf over the same period (Gourmelen et al., 2017). ~~As this ratio was one of the tuning targets for LADDIE (App. B), the average melt rates~~ We found that this regional melt enhancement can be reproduced by LADDIE, conditional on the tuning. Whether the melt enhancement in the Kohler grounding zone are well simulated by this model. ~~In contrast, the MITgem model underestimates the basal melt rates in this region, simulating comparable melt rates to the Crosson-Dotson average values.~~ is realistically simulated thus depends primarily on the model resolution and the choice of  $D_{min}$ .

### 3.1.2 Inter-model comparison

In some regions of the Crosson-Dotson ice shelf, observations are either absent or inconclusive. In these regions, it is worthwhile to compare the simulated melt rates of LADDIE to output from the 3D ocean model MITgem. The primary regions where observations are absent are the grounding zones of the Smith and Pope glaciers. In these grounding zones, both models simulate enhanced melt rates comparable to those in the Kohler grounding zone. The simulated melt in these grounding zones mainly differs between the two models at small-scale detail; this difference arises from the higher spatial resolution of LADDIE.

~~Remote~~ In the shallow regions, the observations are inconclusive with regard to melt or refreezing. In these regions, both models produce weak positive basal melt rates, supporting the assessment that the observed refreezing rates are unrealistic. Overall, the large-scale melt patterns of LADDIE and MITgcm are similar and consistent, providing confidence that the simulated physics is consistent as well.

505 ~~Another region where remote~~ sensing products do not provide reliable estimates for basal melt ~~is~~ at the grounding line, ~~as~~. ~~Remote sensing observations rely on~~ the assumption of flotation ~~fails at this point~~, an assumption which fails near the grounding line. However, ~~numerical ice sheet modeling has been used to conclude that high basal in-situ observations are~~ available from the neighbouring Thwaites grounding line (Davis et al., 2023). These observations revealed low melt rates in grounding line regions with a relatively flat ice shelf base. Both MITgcm and LADDIE reproduce these low melt rates at ~~the~~ 510 ~~grounding line are a necessary ingredient to reproduce the observed grounding line retreat of the Kohler and Smith glaciers (Lilien et al., 2019). The grounding line melt rates simulated by MITgcm are flat~~ grounding line regions. A major difference between the models arises at specific grounding line regions with a steep topography. MITgcm simulates near-zero ~~due to the lack of a simulated barotropic flow through the thin water column. In contrast, high melt rates are~~ melt rates along the complete grounding line, whereas LADDIE simulates high melt rates at these locations of steep topography. The low melt 515 rates of MITgcm may be caused by the coarse vertical resolution or by a limited barotropic flow along the grounding line. The comparably high grounding line melt rates in LADDIE are strongly influenced by the model parameter  $D_{min}$ . Whether the localised high melt rates simulated by LADDIE ~~at the deepest points of the grounding line~~, ~~as this model is unrestricted by the water column thickness. The aforementioned modeling study suggests that significant, non-zero~~ are realistic, cannot be asserted from presently available observations. Hence, the grounding line is a region where the models, at least in their current 520 setup, are inherently inconsistent.

The last region where we compare LADDIE to MITgcm is the Crosson shear margin (Fig. 3m–p). Ice shelf shear margins are often strongly damaged. This damage breaks the assumption of continuity, a central assumption in the computation of basal melt rates ~~may be present at the deepest grounding lines. However, observation-based evidence is required to decide which basal melt pattern (MITgcm or LADDIE) is most realistic in this region~~ from altimetry; in these damaged shear margins, therefore, 525 remote sensing observations are unreliable. Both MITgcm and LADDIE simulate enhanced melt rates along the coastline of Bear Peninsula. A marked difference between melt patterns from LADDIE and MITgcm appears near the ice shelf front. LADDIE simulates relatively high melt rates in the region where the melt plume exits the ice shelf cavity. In contrast, MITgcm simulates low melt rates and does not show a trace of a melt plume here. Melt plumes near ice shelf fronts have been identified indirectly by the presence of polynyas (Alley et al., 2016). Such polynyas are observed throughout the Amundsen Sea region, 530 including the Crosson shear margin. This proxy thus provides evidence that the LADDIE melt pattern in the Crosson shear margin is qualitatively realistic. As shear margins are crucial for ice shelf stability (Sun et al., 2017; Lhermitte et al., 2020), the inconsistency between the melt patterns between MITgcm and LADDIE could be significant in the field of ice shelf modeling.

### 3.1.3 New features

535 The high-resolution simulations with LADDIE reveal a variety of small-scale melt patterns that cannot be confirmed by either observations or inter-model comparison. Here, we describe these new melt features and assess the potential underlying physics.

The high spatial resolution of LADDIE allows it to simulate the channelisation of melt plumes in a number of regions. One example is the Kohler grounding zone. Through the middle of ~~the~~-this grounding zone, LADDIE simulates several elongated melt features. ~~This agrees with the high spatial variability in basal melt rates observed in both the~~ Similar to the Dotson Channel, these channels are carved out in the basal topography of the ice shelf (Fig. 3i). The presence of such channels in both Kohler and Smith grounding zones (Khazendar et al., 2016). These enhanced melt rates align with topographic channels (Fig. ??a), is supported by the high spatial variability in basal melt rates from radar observations (Khazendar et al., 2016). The melt channels appear not to be connected to the grounding line itself, but to originate downstream from the grounding line. Although this ~~may~~-disconnection may very well be an artefact of the smoothing applied to the topography (Sec. 2.3.1), it agrees with the 540 assessment by Alley et al. (2016) that melt channels in this warm region are predominantly ocean-sourced. Such ocean-sourced channels require a locally enhanced basal melt to originate and persist. We see that LADDIE simulates enhanced basal melt in these channels, indicating that the modeled basal melt patterns can support ocean-sourced basal channels.

### 3.1.4 **Dotson Channel**

~~Dotson Channel melt rates. Detailed features within the inset DC in Fig. ??.~~ Note the different colour scale for the ice shelf draft. 550

~~Next, we zoom in on the Dotson Channel and its surroundings (Fig. ??). Comparing the centerline of the topographic channel (Fig. ??a) to the centerline of the observed melt plume (Fig. ??b) reveals a misalignment. The highest melt rates are observed on the western side of the topographic channel. Along the eastern flank of the channel, melt rates are near-zero. This western intensification hints at a significant impact of the Coriolis deflection. The location of the melt peak with respect to the topographic channel is highlighted in Fig. 4 for three cross-sections. In each of the three sections, the Dotson Channel melt peak from both observations and LADDIE are similarly intensified on the western flank.~~ 555

~~Cross sections across the Dotson and Coastal Channels. The location of sections A, B, and C are indicated in Fig. ??. Top row: geometry including the ice shelf (white), ocean cavity (blue), and solid earth (grey). The vertical lines indicate the topographic locations of the channel centerlines. Bottom row: Observed and simulated basal melt rates across the same sections.~~ 560

~~Due to ice-ocean interactions, this western intensification can lead to a westward migration of the channel (Gladish et al., 2012). The asymmetric shape of the topographic channels, with a steeper slope on the left than on the right, indicates that the western intensification of basal melt has already impacted the ice shelf basal topography (Sergienko, 2013). As the location of the melt peak simulated by LADDIE agrees well with that of the observed melt peak, we are confident that the 2D flow of meltwater below the ice shelf, and its Coriolis deflection, is realistically simulated by LADDIE. Due to the relatively coarse resolution of MITgem, this westward intensification cannot be simulated by this 3D model.~~ 565

Closer to the coast of the Dotson Channel, the ice shelf topography reveals another channel, which Another new feature we observe is located to the west of the Dotson Channel. Along the coastline, high melt rates reveal the presence of another narrow channel; we will call this the Coastal Channel (Fig. ??a3h). This channel appears to form a boundary current that converges with the main Dotson Channel flow near the ice shelf front. Along this coastline, observations are again uncertain, as they rely on the assumption of flotation. It is therefore difficult to detect a clear melt signal along this coastal channel originates in the Kohler Grounding Zone and merges with the Dotson Channel before it reaches the ice shelf front. The Coastal Channel is clearly visible in the geometry, in both the plan view (Fig. 3e) and the cross-sections (Fig. ??b). In addition, 4). Although the geometry is also uncertain as it is within 3 km from uncertain near the grounding line. However, the cross-sections reveal a clear topographic Coastal Channel (Fig. 4). Across sections A and B, this channel is sharp and the simulated melt peak by LADDIE aligns with the centerline of, the topographic channel, as the coastal boundary prevents a westward intensification. Across section C, existence of this Coastal Channel can be explained physically. It is likely that meltwater from the Kohler grounding zone is transported to the ice shelf front in the form of a melt plume. This melt plume would be forced towards the western coastline by Coriolis deflection, forming a boundary current. The enhanced melt rates would deepen the topographic channel, keeping the melt plume in place. In addition, this coastal region is a shear margin, in which ice divergence can facilitate the formation of melt channels (Alley et al., 2019). We thus consider the Coastal Channel has detached from the coast and has widened. Across this section, both observations and simulations show a similar westward intensification of the Coastal Channel melt peak, comparable to the Dotson Channel. Whether the Coastal Channel is realistic or an artefact of uncertainty in the topography cannot be determined in this study. However, the sharpness of the channel topography and of the melt peak may indicate that ice-ocean interactions have played a role in shaping the channel topography; if this is the case, LADDIE simulates a physically consistent narrow melt channel. As these elevated melt rates align with the shear margin of the Dotson Ice Shelf, they have a large potential to affect the ice shelf stability,  
and the enhanced melt within it, to be a realistic feature.

The Dotson and Coastal Channels function as conduits for meltwater produced in the deep grounding zones. Looking back at the ice shelf-wide melt patterns shelf-wide melt patterns simulated by LADDIE (Fig. ??3d), we can distinguish two meltwater pathways. The Dotson Channel appears to provide a pathway for meltwater from the Smith grounding zone. Similarly, the Coastal Channel appears to act as the main pathway for meltwater from the Kohler grounding zone. Near the ice-shelf front, these meltwater plumes converge before exiting the ice shelf cavity. Although these two pathways are clearly carved in the ice shelf topography (Fig. ??3a), the remote sensing estimates of basal melt (Fig. ??3b) do not provide conclusive evidence for their existence.

### 3.1.4 **Crosson shear margin**

Crosson Shear margin melt. Detailed features within the inset CS in Fig. ??. Note the different colour scale for the ice shelf draft.

The last melt pattern we highlight on the Crosson-Dotson Ice Shelf is the Crosson shear margin (Fig. ??). Ice shelf shear margins are often strongly damaged. As a consequence, the assumption of continuity — central to the translation of altimetry to

basal-melt rates — breaks down. The observations in shear margins are therefore unreliable. Yet indirect evidence from polynya activity points to the presence of a melt channel along the western boundary of the Crosson ice shelf, extending to the ice-shelf front (Alley et al., 2016). Indeed, away from the ice-shelf front, observations reveal enhanced melt rates in the shear margin along the coastline of Bear Peninsula (Fig. ??b).

605 This enhanced melt along the Bear Peninsula is simulated by both MITgem and LADDIE (Fig. ??c,d). Tracing this melt peak simulated by LADDIE upstream toward the grounding line, we find its origin in the deep Pope grounding zone (Fig. ??d). A meandering melt channel provides a pathway for a melt plume from Besides the two meltwater pathways exiting the Dotson ice shelf front, the melt patterns simulated by LADDIE reveal a third meltwater pathway. A clear melt channel connects the Pope grounding line, past the coastline of Bear Peninsula, all the way to the ice-shelf front. Near the ice-shelf front, enhanced

610 melt rates are observed that hint at a warm melt plume that has the potential to form a polynya. In contrast, the MITgem model simulates no melt at the ice-shelf front and the melt channel is directed away from the shear margin toward the interior of the ice shelf (Fig. ??e).

The enhanced melt rates in shear margins can lead to thinning and weakening of the ice shelf; this results in an increase in damage and a reduction in the buttressing effect. In addition, enhanced melt rates at the ice-shelf front, as indirectly observed by polynya activity, can facilitate a retreat of the ice-shelf front. The relatively far inland position of the Crosson ice-shelf front near Bear Island (Fig. ??a), compared to the rest of the Crosson ice front, hints at high ice-shelf front retreat rates in the past. An accurate simulation of the melt plume pathway from grounding line to ice-shelf front through shear margins is therefore essential for the realistic assessment of ice-shelf stability. zone to the Crosson ice shelf front. Like most melt plumes, this melt plume is channelised by the shape of the basal ice shelf topography. The apparently strict separation of the three pathways

620 may have implications for meltwater forcing of the deep ocean.

The pathway of meltwater from the Pope grounding zone illustrates a separation between the Crosson and Dotson cavities. As discussed in Sec. ??, the meltwater from the Smith grounding zone exits the cavity through the Dotson Channel. However, the ice flow from both Pope and Smith glaciers exit through the Crosson ice shelf. This separation creates an indirect connection between the Pope and Smith glaciers. The meltwater plume from the Pope glacier leads to a weakening of the Crosson shear margin, reducing buttressing and enhancing the ice flow from both Pope and Smith glaciers. The meltwater pathways thus introduce an inter-dependency of the stability of these two glaciers.

625

### 3.2 Filchner-Ronne

### 3.2 Filchner-Ronne

The second ice shelf we use as a test case for LADDIE is the Filchner-Ronne Ice Shelf. For this ice shelf, we take the same values for the tuning parameters as for Crosson-Dotson, yet we adapt the forcing to the generic Weddell Sea climate (see Sec. 2.3.2). The structure of this section is the same as for Crosson-Dotson: we first evaluate the model by comparison to observations, then perform an inter-model comparison to a 3D model, and finally discuss several new melt features.

630

### 3.2.1 Large-scale patterns

#### 3.2.1 Model evaluation

635 The basal melt rates of the ~~Filchner-Ronne~~ Filchner-Ronne Ice Shelf are considerably lower than those of the ~~Crosson-Dotson~~ Crosson-Dotson Ice Shelf. Observations indicate a mean-spatial average melt rate of  $0.32 \pm 0.1 \text{ m yr}^{-1}$  (Rignot et al., 2013). This mean-average melt rate is well-reproduced by ~~both the 3D model NEMO ( $0.33 \text{ m yr}^{-1}$ , Hausmann et al. (2020)) and by~~ LADDIE ( $0.26 \text{ m yr}^{-1}$ ). This agreement implies that LADDIE may be applied to a wide range of ice shelves using a single set of tuning parameters. This reveals an advantage of LADDIE compared to simple basal melt parameterisations, which often  
640 require retuning of the melt sensitivity when applied to different ice shelf regions (e.g., Reese et al., 2018a; Jourdain et al., 2020; Burgard et al., 2020). Besides making the model easier to use, this finding provides some confidence that, in terms of the overall melt sensitivity, the dominant physical mechanisms are represented by LADDIE.

~~Similar to Crosson-Dotson~~ Similar to Crosson-Dotson, the highest basal melt rates of Filchner-Ronne are found in the deep grounding zones (Fig. ~~??5b~~). In contrast to ~~Crosson-Dotson~~ Crosson-Dotson, however, these grounding zone melt rates are  
645 not driven by the presence of warm Circumpolar Deep Water. The ~~Filchner-Ronne~~ Filchner-Ronne Ice Shelf cavity is isolated from intrusions of this warm water mass ~~and is instead~~. Instead, this cavity is forced by waters at the surface freezing point, formed by sea-ice formation offshore (Nicholls et al., 2009); it is therefore classified as a cold cavity. ~~The~~ Rather than warm cavity waters, the high melt rates in the grounding zone are caused by the low freezing point at depth. This freezing point, which can reach values of  $-2.5^\circ\text{C}$ , is substantially lower than the surface freezing point of approximately  $-1.9^\circ\text{C}$ . The ambient  
650 waters within the ~~Filchner-Ronne~~ Filchner-Ronne cavity consist of a mixture of water at surface freezing temperature, and ~~melt water created~~ colder meltwater released at depth. This mixture is warmer than the local freezing temperature within the deep grounding zones. ~~This temperature difference creates a thermal forcing leading to melt rates within the grounding zone of rates up to  $10^{-1}$ , leading to positive melt rates. These show a maximum in the deepest grounding zones where the pressure freezing point reaches a minimum.~~

655 The magnitude of the basal melt rates in the grounding zones of Filchner-Ronne is subject to discussion; this complicates the quantitative evaluation of these regional melt rates simulated by LADDIE. Remote sensing estimates, like those in the Rutford Grounding Zone (Fig. 5i-l), are of the order of  $5 \text{ m yr}^{-1}$  (Rignot and Jacobs, 2002). ~~The simulated melt rates by LADDIE are of a comparable magnitude. However, in-situ observations in the Rutford Grounding Zone estimate substantially lower basal melt rates of approx.  $1 \text{ m yr}^{-1}$  (Jenkins et al., 2006). Further observational research should focus on reconciling these lines of~~  
660 evidence, before LADDIE can be evaluated more robustly in this region. It is, however, noteworthy to mention that grounding zone melt rates in LADDIE are closely tied to the tuning parameter  $D_{min}$ . Lower values of grounding zone melt from in-situ observations can thus be approached by reducing this tuning parameter.

~~As the meltwater at these coldest temperatures~~ As the cold meltwater produced in the deepest grounding zones rises toward the ice-shelf front, the local freezing point increases. At a certain depth, ~~the~~ this meltwater, mixed with ambient water due to  
665 entrainment, ~~is becomes~~ is becomes colder than the local freezing freezing point. At this depth, the thermal forcing becomes negative point. This reversed temperature difference sets up a negative thermal forcing, inducing freezing at the ice shelf base. This pro-

cess, with melt in the deep grounding zone and freezing at intermediate depths, is called the ice pump effect. ~~Observations of marine ice reveal a number of regions with dominant basal freezing: north of~~ The remote sensing observations reveal widespread basal freezing across the central ice shelf (Fig. 5b), a finding that is supported by observations of marine ice (Sandhäger et al., 2004; Holland et al., 2007). Qualitatively, LADDIE reproduces basal freezing in the central ice rises shelf, north of Fowler ~~peninsula, and in the western boundary regions~~ Peninsula, and along the western boundaries of both the Filchner and Ronne ~~Ice Shelves~~ (Sandhäger et al., 2004; Holland and Feltham, 2005; Holland et al., 2007). Both the 3D model as well as LADDIE qualitatively reproduce basal freezing in these regions ~~ice shelves~~ (Fig. ??e,5d). ~~Quantitatively, LADDIE simulates weaker refreezing north~~ These results indicate that the flow direction and cooling of the meltwater plumes originating in the deep grounding zones are well simulated.

Quantitatively, however, a number of discrepancies emerge between LADDIE and observations in the central ice shelf. North of the ice rises, ~~which is partly caused by the idealised, uniform tidal forcing of the model,~~ basal refreezing is underestimated, whereas basal melting is underestimated at the southern point of Berkner Island. Both freezing and melt patterns in these regions have been shown to be enhanced by tidal forcing (Hausmann et al., 2020). Hence, the biases in the LADDIE simulations may be reduced by forcing the model with a spatially heterogeneous tidal forcing. In addition, the freezing and melt patterns in these central regions are likely influenced by the barotropic circulation of water masses (e.g., Naughten et al., 2021). The underestimation of spatial variability in basal melt and freezing by LADDIE may thus partly be caused by the assumption of a stationary ambient ocean, as discussed by Holland et al. (2007).

~~Further downstream, net melt rates are observed~~ Another discrepancy between observations and LADDIE simulations is found along the ice shelf front (Fig. ??b). ~~These melt rates are reproduced by the 3D model, but not by LADDIE. The local enhancement of melt along the~~ Here, LADDIE simulates low melt rates, except for the freezing rates along the western boundaries. The observations, however, show positive melt rates along the entire ice shelf front ~~is caused by the circulation of warmer water within the cavity and by~~. Melting at the ice shelf front is in part attributed to local peaks in tidal velocities (Makinson et al., 2011; Hausmann et al., 2020). ~~The highly idealised forcing of LADDIE lacks these spatial patterns, which at least partly explains the lack of simulated~~ In addition, basal melt at the ice shelf front may be exacerbated by intrusions of a relatively warm water mass into the cavity. This water mass is likely surface-warmed, increasing the ambient temperature in the upper layers (Stewart et al., 2019). ~~The lack of ice shelf front melt in LADDIE. We note that a more detailed forcing, including 3D fields of ambient temperature and salinity, and a non-uniform 2D field of tidal velocities, may improve the spatial patterns of basal melt and freezing by LADDIE~~ melting in LADDIE can thus at least partly be explained by the idealised forcing, which does not represent a spatial variability in tidal velocities or a warm upper-ocean layer. Altogether, with these simulations, a number of discrepancies occur, which may be caused by missing model physics or by overly idealised forcing fields. However, ~~we deem it to be a significant result that the qualitative large-scale patterns of~~ without retuning and with idealised forcing, LADDIE reproduces the average melt rate, the melt maximum in grounding zones, and refreezing in the central regions and western boundaries. This result provides some confidence that LADDIE represents the dominant physical mechanisms governing basal melt and freezing ~~can be reproduced using simple 1D forcing fields and uniform tidal velocities of the Filchner–Ronne Ice Shelf.~~

### 3.2.2 Rutford grounding zone Inter-model comparison

Rutford Grounding zone melt. Detailed features within the insets in Fig. ??.

705 Similar to Crosson-Dotson, the highest basal melt rates on the Filchner-Ronne Ice Shelf are found in the deep grounding zones. One example of these is the Rutford Grounding Zone (Fig. ??). Compared to the Kohler Grounding Zone (Fig. ??b), the observed basal melt rates in the Rutford Grounding Zone are of poorer quality. Similar to Crosson-Dotson, a major inter-model difference is found at the grounding line of Filchner-Ronne. Along the grounding line, the 3D ocean model NEMO simulates near-zero melt rates, whereas LADDIE simulates the highest melt rates at the grounding line (Fig. ??b). This observed basal melt field does not reflect detailed channelised patterns that are clearly visible in the ice shelf topography (Fig. ??a). However, these observations do show an overall pattern of high basal melt rates close to the deepest grounding line, and lower basal melt rates toward the shallower regions. This pattern is confirmed by in-situ observations (Jenkins et al., 2006) as well as estimates from remote sensing (Rignot et al., 2013; Moholdt et al., 2014). These highest basal melt rates near the grounding line occur due to the low freezing temperature and the steep slope of the ice shelf draft. The low freezing temperature enforces a relatively high thermal forcing. In addition, the steep slope facilitates a rapid meltwater flow and a high turbulent exchange of heat toward the cold ice shelf base. Regarding the magnitude of the basal melt rates near the grounding line, in-situ observations have revealed an overestimation of remote sensing-based estimates (Jenkins et al., 2006). LADDIE largely reproduces the near-grounding line basal melt estimates by remote sensing (approx.  $5 \text{ m yr}^{-1}$  to  $5 \text{ k.l}$ ). As described in Sec. 3.1.2, the absence of grounding line melt in a 3D model may be caused by the limited circulation and/or to the vertical resolution of the model. Observational evidence of melt near a grounding line is available for the Rutford Grounding Zone from radar measurements Jenkins et al. (2006). These observations located the highest melt rates at the sites furthest upstream (closest to the grounding line), in-situ observations in the Rutford Grounding zone estimate basal melt rates of approx.  $1 \text{ m yr}^{-1}$ . The basal melt rates by LADDIE nearby grounding lines are strongly tied to the parameter  $D_{min}$ . Tuning down this parameter may reduce the overestimation by LADDIE in this region, hinting at significant grounding line melt as simulated by LADDIE. However, to assess whether LADDIE or NEMO produces the most realistic grounding line melt patterns requires more observational evidence.

710  
715  
720  
725

In contrast to LADDIE, the 3D model NEMO simulates a spatial melt peak at Further downstream, to the mouth of the Rutford Grounding Zone, LADDIE and NEMO simulate a contrasting melt gradient (Fig. 5k,l). LADDIE simulates a gradual decrease in melt from the grounding line to the mouth of the grounding zone; this melt pattern is in qualitative agreement with remote sensing estimates (Rignot et al., 2013; Moholdt et al., 2014; Adusumilli et al., 2020). In the NEMO simulations, however, melt rates increase toward the mouth of the grounding zone. This melt peak pattern is reflected in other grounding zones of the Ronne Ice Shelf (Fig. ??e) is induced by the tidal forcing, which locally increases the thermal forcing (Hausmann et al., 2020). A similar tide-induced peak near the mouth of the grounding zone was simulated using a global setup of the 5c). These melt peaks at grounding zone mouths may be related to an erroneous peak in tidal velocities. Simulations by Padman et al. (2018) showed that these melt peaks can be removed by an observation-based correction of tidal velocities through modifying the bathymetry near grounding zone mouths. This difference between NEMO and LADDIE is thus likely

730  
735

the result of the different tidal velocities, rather than model dynamics. As neither model simulation contains a fully realistic tidal velocity field, no fully realistic melt patterns may be expected from either model.

740 A region where NEMO and LADDIE produce comparable melt patterns that are in disagreement with observations is the Western Boundary of the Ronne Ice Shelf (Fig. 5e-h). Both models simulate a boundary region with basal freezing all the way to the ice shelf front. However, observations show basal melting near this ice shelf front. As shown by simulations by Hausmann et al. (2020) and Padman et al. (2018), this basal melt cannot be explained by the presence or absence of tides. In addition, the basal freezing is retained when the cavity circulation is explicitly solved in a 3D NEMO model (Mathiot et al., 2017). However, Padman et al. (2018) showed that this tidal peak is induced by errors in topography used in barotropic models to resolve tides. They further revealed that these tidal peaks are not in accordance with in situ tidal observations. To resolve this, they corrected for the water column thickness in the grounding zones, thereby removing the tidally induced melt peaks. After this topographic correction, their simulations of basal melt showed the highest basal melt rates in the Rutford grounding zone near the grounding line; this was the case with and without tidal forcing. In conclusion, we consider the simulated tidal peak (Fig. ??c) an unrealistic feature. model, either regionally (Hausmann et al., 2020) or globally (Mathiot et al., 2017). Simulations that do resolve basal melt at this ice shelf front overestimate the extent of basal melt along both the western 750 boundaries of the Ronne and Filchner ice shelves (Richter et al., 2022). The extent of basal melting and freezing along these western boundaries, and the underlying physics determining this extent, is therefore a remaining issue to be resolved by the wider ocean modeling community.

### 3.2.3 New features

The topography of the Rutford grounding zone (Fig. ??a5i) contains a number of channels extending from the deepest grounding 755 line to the mouth of the grounding zone. Along these channels, LADDIE simulates enhanced melt rates (Fig. 5l). As revealed by Alley et al. (2016), the basal channels in the grounding zones of Filchner-Ronne-Filchner-Ronne are primarily subglacially sourced. This implies that subglacial meltwater forms these channels in the grounded parts of the glacier, and these channels means that these channels are formed by subglacial meltwater at the base of the grounded ice, and are advected into the ice shelf as the ice begins to float. In contrast to the suspected ocean-sourced basal melt channels of the Crosson-Dotson 760 Crosson-Dotson Ice Shelf, subglacially sourced channels can persist without enhanced basal melt. The simulated enhanced melt rates along these channels as simulated by LADDIE, however, can aid their persistence and potentially contribute to their westward migration as described in Sec. ?? In order to simulate subglacially sourced channels in a coupled setting, LADDIE should be forced with subglacial meltwater. 3.1.3.

The basal melt patterns simulated by LADDIE (Fig. ??d) propose 5l suggest an enhanced ice pump mechanism within these 765 basal channels. Near the grounding line, melt rates are increased within the channel, compared to inside the channel exceed those outside the channel. This effect is similar to the The mechanism governing this pattern resembles the one governing the high melt rates in ocean-sourced basal channels; increased. Increased melt arises due to the convergence of meltwater plumes and the consequential locally enhanced turbulent exchange. However, further of heat toward the ice shelf base. Further downstream, toward the mouth of the grounding zone, the ice shelf draft within the channels is becomes shallower than outside

770 ~~these channels. Hence~~the channels. As a result, the freezing temperature within the channel is higher than outside, leading to a lower thermal forcing within the channel. Toward the grounding zone mouth, the simulated basal melt within the channels is therefore weaker than outside the channels;~~this~~. This reversing contrast in basal melt rates implies an erosion effect of basal melt on these subglacially sourced channels. A similar erosion of basal channels was found in the Pine Island Ice Shelf (Dutrieux et al., 2013) as well as in idealised coupled ice–ocean modeling (Gladish et al., 2012). We postulate that this erosion effect contributes to the absence of channels in the shallower parts of the ~~Filchner–Ronne~~Filchner–Ronne Ice Shelf. ~~Note that this erosion effect is not present in the small, warm ice shelves like Crosson–Dotson, where ocean-sourced meltwater plumes extend to the ice shelf front. Throughout the whole length of these ice shelves, basal melt rates are enhanced compared to outside the channels.~~

### 3.2.4 ~~Western Boundary~~

780 ~~Western Boundary melt. Detailed features within the insets in Fig. ??.~~

~~Along both Western Boundaries of the Filchner and Ronne Ice Shelves, marine ice is detected (Sandhäger et al., 2004; Holland and Feltham, 2002); this indicates basal freezing. And indeed, observations and model simulations reveal basal freezing along these western boundaries (Fig. ??b,c,d). However, a discrepancy is visible toward the Ronne Ice Shelf front. Here, observations indicate basal melting of the ice shelf. Another feature of LADDIE in the Filchner–Ronne Ice Shelf is basal freezing within a large crevasse (Fig. ??b), whilst both NEMO and LADDIE simulate basal freezing all the way to the ice shelf front (Fig. ??c,d). As shown by simulations by Hausmann et al. (2020) and Padman et al. (2018), the presence or absence of tides cannot explain basal melt at this ice shelf front. In addition, the basal freezing is retained when the cavity circulation is explicitly solved in a 3D model, either regionally (Hausmann et al., 2020) or globally (Mathiot et al., 2017). In contrast, simulations that do resolve basal melt at this ice shelf front overestimate the extent of basal melt along both the western boundaries of the Ronne and Filchner ice shelves (Richter et al., 2022). The extent of basal melt and basal freezing along these western boundaries, and the underlying physics determining this extent, is therefore a remaining issue to be resolved by the wider ocean modeling community. What is relevant for our current study is the consistency between 3D ocean models and LADDIE. LADDIE should be interpreted as a simplified model with less physics at a higher resolution compared to 3D ocean models. Hence, LADDIE is not a suitable model to solve this discrepancy between observed basal melt and simulated basal freezing. Rather, 3D ocean models should be used to assess the physics underlying this basal melt. Processes such as polynya formation and summer solar heating in front of an ice shelf (Stewart et al., 2019) can induce basal melt near ice shelf fronts. When simulated correctly using a 3D ocean model, this process will be reflected in the ambient temperature and salinity fields produced by that model. These fields can then be used to force the LADDIE model in order to check whether the basal freezing at the ice shelf front can be removed.~~

800 ~~Near the ice shelf front of the Ronne Ice Shelf, a large crevasse exists (Fig. ??a). The observations show slightly elevated basal melt in this region (Fig. ??b). In contrast, previous modeling studies indicated net freezing in crevasses due to frazil ice formation (Jordan et al., 2014). The 3D model results do not resolve any spatial variations in basal melt or freezing at this scale (Fig. ??c). 5e,h). This basal freezing is in agreement with previous studies (Khazendar and Jenkins, 2003; Jordan et al., 2014)~~

Within the crevasse, LADDIE simulates enhanced basal freezing. Here, two factors are at play. Within the crevasse, the relatively shallow ice shelf base enforces a relatively high pressure melting point is relatively high, creating; this creates a large negative thermal forcing. In addition, the steep slopes around the crevasse allow for a strong turbulent exchange. The latter factor can also explain the slightly elevated basal melt in the observations, creating an enhanced turbulent exchange in a region of positive thermal forcing. This is in line with the discrepancy described above, that the ambient temperatures near this ice shelf front are likely higher than those prescribed as forcing to LADDIE. Based on this, we argue that more realistic forcing fields could improve the simulated basal melt rates by LADDIE in this region near the Ronne Ice Shelf front. Marine ice freezing can limit the propagation of crevasses and can hence slow down calving processes (MacAyeal et al., 1998). The significance of this effect should be quantified in a high-resolution coupled modeling study in which basal freezing in crevasses is resolved.

#### 4 Discussion

In the quest for a computationally efficient method to simulate physically plausible basal melt fields, we have presented the 2D model LADDIE. The model can be seen is developed as a tool to simulate basal melt rates that sits between computationally cheap, yet physically more idealised parameterisations and physically more realistic, yet computationally heavy 3D ocean models. The potential relevance of LADDIE to the field of ice sheet modeling relies depends on its ability to combine the strengths of parameterisations and 3D ocean models. This means that the model must be computationally significantly cheaper than 3D models whilst producing significantly more realistic basal melt fields than idealised parameterisations.

In terms of its computational cost, LADDIE falls in between simple parameterisations and 3D ocean models. Basal melt parameterisations (e.g., Reese et al., 2018a; Jourdain et al., 2020) (e.g., Favier et al., 2019; Reese et al., 2018a; Lazeroms et al., 2019; Jourdain et al., 2020) can be computed online with negligible computational cost. In contrast, 3D ocean models require considerable resources; for that reason, the resolution in the ISOMIP+ protocol was adjusted from  $1 \times 1$  to  $2 \times 2$  km<sup>2</sup>. The higher resolution would pose a significant limitation to the participation of 3D ocean models (Asay-Davis et al., 2016). For LADDIE at a  $1 \times 1$  km<sup>2</sup> resolution, a full spin up requires 0.5 CPU hours for the ~~Crosson-Dotson~~ Crosson-Dotson Ice Shelf and 60 CPU hours for the ~~Filchner-Ronne~~ Filchner-Ronne Ice Shelf. This computational advantage allows for the configuration at a higher resolution, hence resolving more spatial detail. In addition, the difference in the relatively low computational cost makes LADDIE particularly suitable for extensive tuning and sensitivity experiments, for which a large number of simulations are is required.

The spatial detail of the basal melt fields simulated by LADDIE are is of comparable quality to those that produced by 3D ocean models. A particular improvement compared to basal melt parameterisations (e.g., Burgard et al., 2022) is that LADDIE resolves the influence of ice shelf topography and Coriolis deflection on the meltwater flow. This allows for the simulation of physically plausible enhanced melt rates in basal channels and shear zones, as well as the western intensification of basal melt plumes melt within basal channels. Each of these features can have a significant effect on ice shelf dynamics and thus on ice-ocean interactions. In comparison to 3D ocean models, LADDIE reproduces most basal melt features despite its idealised physical description. The higher resolution at which LADDIE can be configured allows for more detail in fine-scale features such as basal channels; again, the simulation of these kilometer-scale features. As an example of the resolution-sensitivity of

LADDIE, the tuning procedure is applied to three resolutions (App. B). This tuning revealed that LADDIE can only accurately reproduce the observed melt peak through the center line of the Dotson Channel at 500x500 m resolution. The accurate simulation of such details may be important for coupled ice–ocean modeling. ~~In addition, LADDIE resolves significant basal melt rates at the grounding line. These melt rates may be overestimated for the Filchner-Ronne Ice Shelf (Jenkins et al., 2006), yet are in line with the assessed conditions to reproduce historical grounding line retreat of the Crosson-Dotson Ice Shelf (Lilien et al., 2019), highlighting the need for (sub-)kilometre resolution basal melt patterns.~~

In this study, the main simulations were based on idealised forcing, combining horizontally uniform profiles of temperature and salinity with horizontally uniform values of tidal forcing. As shown for the Crosson-Dotson Ice Shelf in App. A, quantitative improvements can be made to the simulated basal melt fields with 3D temperature and salinity forcing. ~~Despite the computational advantages of LADDIE, a number of inherent limitations are posed by its 2D configuration. For example, the configuration prevents the explicit computation of certain processes such as turbulence, barotropic flow, and heat transfer processes in the complete cavity. In addition, the model design makes LADDIE unsuitable for the study of a number of physical processes related to Antarctic ice shelf basal melt. First and foremost, LADDIE cannot resolve processes governing the heat exchange between the deep ocean and the continental shelf (e.g., Thompson et al., 2018). In addition, spatially non-uniform tidal forcing may improve the basal melt and freezing patterns of the Filchner-Ronne Ice Shelf (Makinson et al., 2011; Hausmann et al., 2020). We caution though that incorrect tidal velocities in grounding zones can obscure melt rates in these regions, unless corrected for as described by Padman et al. (2018). The simulations were performed without subglacial outflow. This external forcing could easily be added as a volume source in Eq. 1 and may affect near-grounding line basal melt rates (Jenkins, 2011). In addition, in coupled ice–ocean settings including LADDIE, subglacial outflow is an essential process that forms topographic channels. For the study of the topographic impact on basal melt, however, we considered idealised forcing profiles to be more illustrative. Based on these, we conclude that a detailed geometry combined with reasonable forcing fields allows for the reproduction of the majority of basal melt patterns the model cannot be used to address questions related to time scales and tipping points related to the cavity circulation (Naughten et al., 2021). Finally, the sensitivity of basal melting to nearby near-surface processes, e.g., solar absorption in polynyas (Stewart et al., 2019), is beyond the model scope. Research questions such as these require 3D ocean models and coupled ESMs to be studied. For such problems, LADDIE can only function to downscale basal melt rates based on output from 3D ocean models.~~

The model version presented here is the first version of the LADDIE model, which can be expanded in a number of ways. One missing aspect is the option for ~~convection-driven melting~~ melting driven by double-diffusive convection in regions where shear-driven melting is absent. This process is inherently difficult to parameterise (Rosevear et al., 2022) and therefore currently not included in the model. Rather, melting in regions with low velocities is ~~induced~~ maintained in LADDIE by ~~enhancing local entrainment in order to ensure a minimal~~ the enforcement of a minimal layer thickness  $D_{min}$ . ~~This process can be replaced when a suitable parameterisation for convection-driven melting is developed.~~ Similarly, the present model version does not account for the impact of double diffusion on the vertical heat exchange (Rosevear et al., 2021) ~~is not included in the present model version.~~ Another process that is currently not included is the limitation imposed by the available water column thickness. In most regions, the plume thickness is significantly less than the total water column thickness. Therefore,

~~no bathymetric constraint is imposed in~~ the present version of LADDIE does not account for any bathymetric constraints. However, the thin water column nearby grounding lines suppresses the horizontal transport of heat which is entrained into the meltwater layer. Limiting this heat transport through bathymetric constraints ~~would could~~ reduce basal melt nearby grounding  
875 lines, ~~possibly reducing the overestimation of basal melt rates in the Rutford grounding zone~~. Future model development and ~~validation evaluation~~ should combine the inclusion of bathymetric constraints with detailed ~~validation evaluation~~ of grounding zone melt to in-situ observations at various ice shelves. Note that this also requires robust bathymetric data which is at present largely unavailable. Finally, basal freezing commonly occurs due to frazil ice formation and deposition (Holland and Feltham, 2005; Jordan et al., 2014). The overall patterns of basal freezing by LADDIE appear physically plausible, yet these may be  
880 improved by explicitly simulating frazil ice formation. All of the above processes are considered possible expansions of the model, beyond the scope of this first model version.

~~Despite the computational advantages of a 2D model, this configuration poses a number of limitations to the applicability of LADDIE. The 2D configuration prevents the explicit computation of certain processes such as turbulence, barotropic flow, and conservation laws in the complete cavity.~~In addition to more advanced physics, the simulated melt patterns can be improved  
885 through more advanced forcing. As shown for the Crosson–Dotson Ice Shelf in Appendix A, forcing LADDIE with 3D temperature and salinity fields can quantitatively improve simulated basal melt fields. In addition, ~~the model design makes LADDIE unsuitable for the study of a number of physical processes related to Antarctic ice shelf basal melt. First and foremost, LADDIE cannot resolve shelf processes governing the heat exchange between the deep ocean and the continental shelf (e.g., Thompson et al., 2018). In addition, the model cannot address questions related to time scales and tipping points related to the cavity circulation (Naughten et al., 2021). Finally, the effects of sea ice, such as solar absorption in polynyas (Stewart et al., 2019), are beyond the model scope. Research questions such as these require 3D ocean models and coupled ESMS to be studied. For such problems, LADDIE can only function to downscale basal melt rates based on output from 3D ocean models.~~ basal melt and freezing patterns of Filchner–Ronne may be improved by spatially heterogeneous tidal forcing (Makinson et al., 2011; Hausmann et al., 2020). We caution though that melt patterns can be obscured by incorrect  
895 tidal velocities in grounding zones, unless these are corrected for as described by Padman et al. (2018). Another possible improvement in the forcing can be the inclusion of subglacial outflow, which was neglected in this study. This additional forcing can easily be added as a volume source in Eq. 1 if robust data are available. Subglacial outflow can affect near-grounding line basal melt rates (Jenkins, 2011). In addition, in coupled ice–ocean settings including LADDIE, subglacial outflow is an essential process that forms topographic channels. As a first model evaluation, however, we considered idealised forcing profiles  
900 to be more illustrative. Based on these, we conclude that a detailed geometry combined with idealised forcing fields allows for the reproduction of the majority of basal melt patterns in both cold and warm environments.

~~Both LADDIE and~~ The basal melt model LADDIE is developed for widespread use. To run the model, a 2D field of the ice shelf geometry is needed, alongside a configuration file in which the forcing and parameter values are specified. For the geometry, realistic input data can be taken from BedMachine (Morlighem et al., 2020). Alternatively, output from an ice sheet  
905 model or an idealised geometry can be provided. An internal routine in the model allows for a coarsening of the geometry to a lower spatial resolution to save computation time. For the forcing, a number of idealised options are included in the model;

alternatively the forcing can be provided as external 1D profiles or 3D ocean models are primarily validated by comparison to observations of basal melt. However, these observations are inherently uncertain. Most observations are indirectly derived from remote sensing estimates of altimetry. Their conversion to basal melt rates relies on estimates of the surface mass balance and the ice flow convergence, combined with the assumption of flotation. Uncertainties in each of these aspects reduce the reliability of estimated basal melt rates nearby grounding lines, in highly dynamical regions such as shear zones, and on small scales such as within kilometer-width channels. Due to these uncertainties, discrepancies between observations and model results do not unequivocally point to model deficiencies. Hence, the limited availability and reliability of observed basal melt rates is one bottleneck for the validation, tuning, fields. The forcing fields of ‘offshore’ temperatures and salinities should be representative of those in the ice shelf cavity below the upper mixed layer. We note that grid coarsening and detailed forcing may be particularly useful for the application to large ice shelves such as Filchner–Ronne. With minor modifications, the model can be adapted to deal with temporally varying geometry or forcing, and development of LADDIE and other 2D fields of tidal velocities, subglacial meltwater forcing, and ice shelf temperatures. Based on the results in this study, we consider the tuning parameters in Table 2 to be widely applicable. If retuning is necessary for future purposes, we propose to use  $C_{d,top}$  to tune to ice shelf average melt rates, and  $D_{min}$  to tune to near-grounding line melt rates. In applications of transient states, rather than a time-mean steady state, the parameter  $\nu$  should ideally be decreased to limit numerical smoothing. Finally, as in 3D ocean models, the scarcity of observations, however, also creates the option to use LADDIE for applications of data assimilation and/or reanalysis, the time step  $\Delta t$ , the viscosity  $A_b$  and the diffusivity  $K_b$  should be adapted to the grid resolution in order to ensure numerical stability.

## 925 5 Conclusions

In this study, we have introduced the basal melt model LADDIE. The model resolves the layer thickness, momentum, temperature, and salinity of the upper ocean layer below ice shelves on a 2D grid. The aim of the model is model is developed to simulate basal melt patterns of comparable quality to 3D ocean models, yet with a considerably lower computational cost which allows, allowing LADDIE to be configured on a finer grid. We have validated/evaluated the model by comparing simulated basal melt fields of the Crosson–Dotson and Filchner–Ronne Crosson–Dotson and Filchner–Ronne Ice Shelves to observations and to remote sensing observations. In addition, the simulated melt fields were compared to output from 3D ocean model output. By resolving topographic steering and Coriolis deflection of the meltwater flow, LADDIE produces significantly more detailed basal melt patterns than parameterisations of lower order models to assess the performance of LADDIE relative to state-of-the-art ocean models. LADDIE realistically simulates the ice shelf average melt rates as well as the large-scale pattern of basal melt/melting and freezing in both warm and cold environments. In addition, LADDIE simulates physically plausible/For large ice shelves such as the Filchner–Ronne Ice Shelf, melt patterns may be improved by increasing the detail in the forcing fields of ambient temperatures and salinities and tidal velocities. LADDIE is able to simulate a number of new small-scale features including basal melt within topographic channels, along shear margins, and nearby grounding lines. Its performance on melt features that are not visible in either observations or 3D ocean models, yet which are consistent with the

940 applied geometry. As these features may impact ice–ocean feedbacks, they emphasise the need for the capability to simulate  
(sub-)kilometre basal melt fields. The performance of LADDIE at these small spatial scales makes the model particularly  
suitable for providing basal melt ~~fields as~~ forcing for high-resolution ice sheet models. We thus conclude that LADDIE can  
function to bridge the resolution gap between ocean models and ice sheet models. The model is freely available and published  
open source. It is relatively easy to use in offline applications with prescribed ice shelf geometries, and can be adapted for use  
945 in coupled settings.

*Code and data availability.* The model code is available on <https://github.com/erwinlambert/laddie>. The code for analysing model output and creating figures is available on <https://github.com/erwinlambert/laddie-description>. The model results are available on <https://zenodo.org/record/8014160>. The BedMachine v2 data is available from <https://nsidc.org/data/nsidc-0756>

## Appendix A: Sensitivity to 3D forcing

950 The LADDIE model can be forced with either 1D profiles of ambient temperature and salinity, or 3D fields representing the cavity. In the main text of this paper, idealised 1D profiles are applied. In this section, we address the impact of 3D forcing. In Fig. A1, melt patterns under both forcing options are shown. The 1D forcing is identical to that described in the paper. The 3D forcing is derived from the MITgcm model over the period 2003–2008.

955 The time-average 3D fields of temperature and salinity are interpolated horizontally onto the LADDIE grid. The upper two grid cells below the ice shelf are removed, as these are assumed to represent the meltwater layer rather than the ambient waters. The profiles are extrapolated vertically to the ice shelf base, and horizontally into missing grid cells. Finally, to ensure smooth and continuous profiles of temperature and salinity, a vertical smoothing is applied with a window of 10 meters. The ambient fields  $T_a$  and  $S_a$  are derived by repeating the interpolation of the 1D forcing method (Sec. 2.3.2) for each horizontal grid cell.

960 Notably, the melt patterns (Fig. A1a,b) show a strong similarity. From large to small scales, melt patterns and plumes are resolved regardless of the forcing field. These patterns are governed by the topography which has a first-order impact on the basal melt patterns. The differences arise primarily in the high-melt region downstream from the Smith grounding zone (higher melt for 3D forcing) and the melt channels and shear zones (lower melt rates for 3D forcing). These differences arise due to the differences in the applied forcing fields, including the stratification therein. We note that a greater overlap between the two cases could be achieved if the 1D forcing profiles were derived directly from the 3D MITgcm fields. However, this comparison shows the difference between the simplest application of the model (idealised 1D forcing) and the most complex one (detailed 3D forcing). Although significant differences exist, the basal melt patterns are nearly identical, implying that the exact forcing has a second order effect. A major exception to this is the average basal melt rate, which is strongly tied to the forcing applied.

970 The above analysis illustrates that basal melt patterns at the scale of the relatively small Crosson–Dotson Ice Shelf are predominantly governed by the ice shelf topography, rather than the distribution of heat and salt throughout the cavity. This conclusion may be less applicable to the larger Filchner–Ronne Ice shelf. Here, the spatial scales allow for a stronger horizontal non-uniformity in the distribution of warm and cold water masses throughout the cavity. Hence, an accurate 3D forcing may have a larger impact on the basal melt pattern of large ice shelves such as Filchner–Ronne.

## Appendix B: Tuning

As described in the main text, we consider two parameters,  $C_{d,top}$  and  $D_{min}$  as tuning parameters. The tuning is based on the ~~Crosson–Dotson~~ Crosson–Dotson simulations with 3D forcing from MITgcm, averaged over the period 2003–2008. For both parameters, we apply a tuning procedure based on five tuning targets described below. The parameters are tuned for three horizontal resolutions, namely  $\Delta x = 0.5$  km, 1.0 km, and 2.0 km. We scale the horizontal viscosity and diffusion linearly with the resolution, leading to values  $A_h = K_h = 25, 50, \text{ and } 100 \text{ m}^2\text{s}^{-1}$  respectively. These latter values were based on trial and error, largely guided by numerical stability.

980 For each resolution, 16 ~~simulates~~ simulations are performed with all combinations of  $C_{d,top} \in [0.8; 1.0; 1.2; \text{and } 1.4 \times 10^{-3}]$  and of  $D_{min} \in [2; 4; 6; 8 \text{ m}]$ . For each of these 16 simulations, the diagnostics described below are quantified. Based on the best fit to the tuning targets, for each of the three resolutions, the optimal values of  $C_{d,top}$  and  $D_{min}$  are extracted.

## B1 Tuning targets

As tuning targets, we consider a range of five diagnostics. The average melt rate over the total ~~Crosson-Dotson~~ Crosson-Dotson Ice Shelf is tuned to a range of 8.7–9.9 m yr<sup>-1</sup>. This range is based on the average melt rate of  $9.3 \pm 0.6$  m yr<sup>-1</sup> derived from  
985 remote sensing observations over the period 2003–2008 by Rignot et al. (2013).

The following three diagnostics represent the spatial melt pattern: The melt rate in the Kohler grounding zone, the Dotson Channel, and the centerline along this Dotson Channel (see Fig. ?? 3 for the locations). The melt rates in these regions are tuned to remote sensing observations over a different period (2010–2016) in order to utilise the data of Goumelen et al. (2017). To  
990 compensate for interannual variability, we tune the model to melt amplifications (regional melt divided by ice-shelf average melt), rather than the actual melt rates. These amplifications were found to be more robust on an interannual basis.

For the Dotson Channel and the centerline along this channel, tuning ranges are derived from the remote sensing observations over the period 2010–2016 by Goumelen et al. (2017), equal to those presented in the main text. Melt amplifications are derived by dividing these regional melt rates by the ~~Crosson-Dotson~~ Crosson-Dotson average melt rate of 6.89 m yr<sup>-1</sup> over 2010–2016  
995 (Goldberg et al., 2019). Note that we follow Goldberg et al. (2019) and average melt rates by omitting negative values. This leads to regional melt amplifications in the Dotson Channel of 1.2 and along the Channel Centerline of 2.8. Without reported uncertainties in the data set, we are forced to prescribe arbitrary uncertainties. We apply tuning ranges of 1.1–1.3 and 2.4–3.2 respectively.

For the Kohler grounding zone, we combine estimates from the same remote sensing data set with estimates from radar  
1000 observations over the comparable period 2010–2014 (Khazendar et al., 2016). The average melt rate over the Kohler grounding zone from remote sensing is 25.5 m yr<sup>-1</sup>. From radar observations, this is 20.4 m yr<sup>-1</sup>. Using these values as upper and lower bounds for the tuning range gives a range for the Kohler amplification of 3.0–3.8.

The fifth and last diagnostic used as a tuning target is the total overturning circulation. The overturning in LADDIE ~~is interpreted~~ can be interpreted in two ways, dependent on the assumption of the fate of detrained water. If this water exits the cavity below the meltwater plume, it is part of the total overturning; if it recirculates in the cavity and re-enters the meltwater layer through entrainment, it is not. Here, we assume the former, and interpret the overturning as the integrated entrainment of ambient water ~~into the upper layer~~. This volume flux, together with the small volume flux of meltwater, exits the meltwater layer through detrainment and outflow across the ice-shelf front. Note that, for Crosson-Dotson, the contribution of detrainment is small and the tuning is independent on the above interpretation. We extract observations from the years 2006, 2007 and 2011  
1010 during which melt rates were comparable to the period 2003–2008 (Jenkins et al., 2018). We take a tuning range based on the lowest and highest observations among these three years, leading to a range of 0.39–0.61 Sv.

## B2 Tuning results

The tuning results are shown in Fig. B1, with the first five columns representing the five tuning targets, and the three rows representing the three resolutions. The coloured shading displays the simulated diagnostic values. The grey shaded zone in each panel marks the tuning range. In the sixth column, the overlap of the five tuning ranges is shown, with darker regions marking a better agreement with the tuning targets.

Based on this overlap, the optimal values for  $C_{d,top}$  and  $D_{min}$  are determined, marked by the yellow dots. For resolutions of 1.0 and 2.0 km, four of the five diagnostics fall within the tuning range, with the Channel Centerline (CC) being the exception. For the resolution of 0.5 km, all five tuning targets are met and a full agreement was found between model and observations.

We find that we can choose the same optimal value for  $C_{d,top}$  for each resolution. This value of  $1.1 \times 10^{-3}$  is close to the value of  $1.0 \times 10^{-3}$ , taken by previous studies (Jourdain et al., 2017; Mathiot et al., 2017). Keeping this same value of  $C_{d,top}$  for all resolutions, we find that differences in resolution – and correspondingly the viscosity  $A_h$  and diffusivity  $K_h$  – can be compensated by varying  $D_{min}$ . Keeping the same parameter values, the average melt and the Kohler amplification decrease when the resolution is increased. Decreasing  $D_{min}$  reduces the thickness of the thermal barrier that the simulated layer forms between the warm ambient water and the ice shelf draft. The consequence is that a reduced value of  $D_{min}$  increases the average melt and the Kohler amplification, thus compensating for the increased resolution.

The single tuning target that cannot be obtained with all resolutions is the Channel Centerline (CC) amplification. The observed range of 2.4-3.2 can only be reproduced using a resolution of 0.5 km (Fig. B1p). Whilst the melt amplification over the full width of the Dotson Channel can be reproduced with each resolution, the sharpness of the melt peak across this channel requires a high resolution and a low viscosity and diffusivity. This finding highlights the importance of high-resolution basal melt patterns. Forcing an ice shelf model with basal melt rates at a too coarse resolution, may underestimate the thinning along the centerline of the channel. This can lead to an underestimation of the time it takes for the channel to 'burn through' the ice shelf (e.g., Gourmelen et al., 2017). The optimal parameter values for each resolution are used throughout the current study for both ~~Crosson-Dotson and Filchner-Ronne~~ Crosson-Dotson and Filchner-Ronne Ice Shelves.

In order to show the robustness of the tuning procedure to the interannual variability, we have performed simulations for each year between 1979 and 2012, using annual mean 3D forcing from the MITgcm simulations (Fig. B2). For the average melt (Fig. B2a), the interannual variability is strong and time periods must be selected carefully, as we have done. For the regional melt applications (Fig. B2b-d) and the overturning circulation (Fig. B2e), the interannual variability is comparable to the assessed uncertainty. Hence, the exact time period used to gather the tuning targets from observations is less important. Based on this, we are confident that the above tuning procedure is robust with respect to interannual variability.

## Appendix C: Pine Island

As additional model evaluation, we have included basal melt patterns for the Pine Island Ice Shelf (Fig. C1). This ice shelf resides nearby Crosson-Dotson in the warm Amundsen Sea Embayment.

1045 The observations (Fig. C1b) are from Shean et al. (2019), using a comparable method based on remote sensing to the  
Crosson–Dotson observations from Gourmelen et al. (2017). The 3D model output (Fig. C1c) is from the same MITgcm  
simulation, over the same period, as described in Sec. 2.2.3. LADDIE is configured with the same model tuning as Crosson–Dotson  
and Filchner–Ronne, at 500 m resolution. Its forcing is nearly identical to that of Crosson–Dotson, with the sole adaptation  
that the temperature at depth is set at 1.0°C and the thermocline depth is set at 450 m, mimicking the observations from  
Dutrieux et al. (2014). The simulation is run for a total of 30 model days, taking 23 CPU minutes.

1050 The average melt rate simulated by LADDIE is  $15.3 \text{ m yr}^{-1}$ , in good agreement with observed estimates from Rignot et al. (2013)  
( $16.2 \pm 1 \text{ m yr}^{-1}$ ) and from Shean et al. (2019) ( $13.1 - 14.9 \text{ m yr}^{-1}$ , converted from  $\text{Gt yr}^{-1}$  using the ice shelf area from  
Rignot et al. (2013)). The total overturning circulation simulated by LADDIE is 0.34 Sv, which falls within the observed range  
of 0.25–0.40 Sv (Dutrieux et al., 2014). Based on these results, we conclude that the model tuning based on Crosson–Dotson  
is applicable to other warm ice shelves as well.

1055 Besides the bulk numbers described above, a close agreement is found between the observed melt pattern (Fig. C1b) and  
the simulated melt patterns by MITgcm (Fig. C1c) and LADDIE (Fig. C1d). A major discrepancy is the deepest grounding  
zone, where both models simulate lower melt rates than the observed values, though the observations are uncertain in this  
region because the ice is not freely floating. A clear overlap between observations and LADDIE is found in the Y-shaped  
channel near the Southern ice shelf front, where melt plumes with enhanced melt rates flow through the channel. In addition,  
1060 a large number of meandering channels are observed and simulated in the center of the ice shelf. These results illustrate that  
LADDIE simulates significantly more realistic melt patterns for Pine Island Ice Shelf than simpler basal melt parameterisations  
(Burgard et al., 2022).

*Author contributions.* EL and AJ conceived the idea of the paper. EL wrote most of the code with significant contributions from AJ. PH contributed to the model physics. All authors contributed to the scoping and writing of the paper.

1065 *Competing interests.* The authors declare no competing interests.

*Acknowledgements.* EL was funded by the Netherlands Organization for Scientific Research (grant no. OCENW.GROOT.2019.091). AJ was funded by the Netherlands Polar Programme and the Water, Climate and Future Deltas program of Utrecht University. The authors thank U. Hausmann for sharing the NEMO output and N. Gourmelen for the remote sensing data of ~~Crosson–Dotson~~Crosson–Dotson. The authors are grateful to T.F. Jesse for the extensive model testing. Finally, the authors thank C. Burgard and one anonymous reviewer for their thorough  
1070 and constructive feedback, which allowed us to significantly improve this work.

## References

- Adusumilli, S., Fricker, H. A., Medley, B., Padman, L., and Siegfried, M. R.: Interannual variations in meltwater input to the Southern Ocean from Antarctic ice shelves, *Nature Geoscience*, 13, 616–620, <https://doi.org/10.1038/s41561-020-0616-z>, 2020.
- Alley, K. E., Scambos, T. A., Siegfried, M. R., and Fricker, H. A.: Impacts of warm water on Antarctic ice shelf stability through basal channel formation, *Nature Geoscience*, 9, 290–293, <https://doi.org/10.1038/ngeo2675>, 2016.
- Alley, K. E., Scambos, T. A., Alley, R. B., and Holschuh, N.: Troughs developed in ice-stream shear margins precondition ice shelves for ocean-driven breakup, *Science Advances*, <https://doi.org/10.1126/sciadv.aax2215>, 2019.
- Asay-Davis, X. S., Cornford, S. L., Durand, G., Galton-Fenzi, B. K., Gladstone, R. M., Gudmundsson, G. H., Hattermann, T., Holland, D. M., Holland, D., Holland, P. R., Martin, D. F., Mathiot, P., Pattyn, F., and Seroussi, H.: Experimental design for three interrelated marine ice sheet and ocean model intercomparison projects: MISMIP v. 3 (MISMIP +), ISOMIP v. 2 (ISOMIP +) and MISOMIP v. 1 (MISOMIP1), *Geoscientific Model Development*, 9, 2471–2497, <https://doi.org/10.5194/gmd-9-2471-2016>, 2016.
- Berger, S., Drews, R., Helm, V., Sun, S., and Pattyn, F.: Detecting high spatial variability of ice shelf basal mass balance, *Roi Baudouin Ice Shelf, Antarctica, The Cryosphere*, 11, 2675–2690, <https://doi.org/10.5194/tc-11-2675-2017>, 2017.
- Bull, C. Y. S., Jenkins, A., Jourdain, N. C., Vaňková, I., Holland, P. R., Mathiot, P., Hausmann, U., and Sallée, J.-B.: Remote Control of Filchner-Ronne Ice Shelf Melt Rates by the Antarctic Slope Current, *Journal of Geophysical Research: Oceans*, 126, e2020JC016550, <https://doi.org/10.1029/2020JC016550>, 2021.
- Burgard, C., Jourdain, N. C., Reese, R., Jenkins, A., and Mathiot, P.: An assessment of basal melt parameterisations for Antarctic ice shelves, *The Cryosphere*, 16, 4931–4975, <https://doi.org/10.5194/tc-16-4931-2022>, publisher: Copernicus GmbH, 2022.
- Carrere, L., Lyard, F., Cancet, M., Guillot, A., and Roblou, L.: FES 2012: A New Global Tidal Model Taking Advantage of Nearly 20 Years of Altimetry, *710*, 13, <https://ui.adsabs.harvard.edu/abs/2013ESASP.710E..13C>, 2013.
- Davis, P. E. D., Nicholls, K. W., Holland, D. M., Schmidt, B. E., Washam, P., Riverman, K. L., Arthern, R. J., Vaňková, I., Eayrs, C., Smith, J. A., Anker, P. G. D., Mullen, A. D., Dichek, D., Lawrence, J. D., Meister, M. M., Clyne, E., Basinski-Ferris, A., Rignot, E., Queste, B. Y., Boehme, L., Heywood, K. J., Anandakrishnan, S., and Makinson, K.: Suppressed basal melting in the eastern Thwaites Glacier grounding zone, *Nature*, 614, 479–485, <https://doi.org/10.1038/s41586-022-05586-0>, 2023.
- Dutrieux, P., Vaughan, D. G., Corr, H. F. J., Jenkins, A., Holland, P. R., Joughin, I., and Fleming, A. H.: Pine Island glacier ice shelf melt distributed at kilometre scales, *The Cryosphere*, 7, 1543–1555, <https://doi.org/10.5194/tc-7-1543-2013>, 2013.
- Dutrieux, P., Rydt, J. D., Jenkins, A., Holland, P. R., Ha, H. K., Lee, S. H., Steig, E. J., Ding, Q., Abrahamsen, E. P., and Schröder, M.: Strong Sensitivity of Pine Island Ice-Shelf Melting to Climatic Variability, *Science*, 343, 174–178, <https://doi.org/10.1126/science.1244341>, 2014.
- Favier, L., Jourdain, N. C., Jenkins, A., Merino, N., Durand, G., Gagliardini, O., Gillet-Chaulet, F., and Mathiot, P.: Assessment of sub-shelf melting parameterisations using the ocean–ice-sheet coupled model NEMO(v3.6)–Elmer/Ice(v8.3), *Geoscientific Model Development*, 12, 2255–2283, <https://doi.org/10.5194/gmd-12-2255-2019>, 2019.
- Feldmann, J., Reese, R., Winkelmann, R., and Levermann, A.: Shear-margin melting causes stronger transient ice discharge than ice-stream melting in idealized simulations, *The Cryosphere*, 16, 1927–1940, <https://doi.org/10.5194/tc-16-1927-2022>, 2022.
- Fox-Kemper, B., Hewitt, H. T., Xiao, C., Aðalgeirsdóttir, G., Drijfhout, S. S., Edwards, T. L., Gollledge, N. R., Hemer, M., Kopp, R. E., Krinner, G., Mix, A., Notz, D., Nowicki, S., Nurhati, I. S., Ruiz, L., Sallée, J.-B., Slangen, A. B. A., and Yu, Y.: Ocean, Cryosphere and Sea Level Change, in: *Climate Change 2021: The Physical Science Basis. Contribution of Working Group I to the Sixth Assessment Report of the Intergovernmental Panel on Climate Change*, pp. 1211–1362, Cambridge University Press, Cambridge, United Kingdom

- and New York, NY, USA, <https://doi.org/10.1017/9781009157896.011>, [Masson-Delmotte, V., P. Zhai, A. Pirani, S.L. Connors, C. Péan, S. Berger, N. Caud, Y. Chen, L. Goldfarb, M.I. Gomis, M. Huang, K. Leitzell, E. Lonnoy, J.B.R. Matthews, T.K. Maycock, T. Waterfield, O. Yelekçi, R. Yu, and B. Zhou (eds.)], 2021.
- 1110 Gaspar, P.: Modeling the Seasonal Cycle of the Upper Ocean, *Journal of Physical Oceanography*, 18, 161–180, [https://doi.org/10.1175/1520-0485\(1988\)018<0161:MTSCOT>2.0.CO;2](https://doi.org/10.1175/1520-0485(1988)018<0161:MTSCOT>2.0.CO;2), 1988.
- Gladish, C. V., Holland, D. M., Holland, P. R., and Price, S. F.: Ice-shelf basal channels in a coupled ice/ocean model, *Journal of Glaciology*, 58, 1227–1244, <https://doi.org/10.3189/2012JoG12J003>, 2012.
- 1115 Goldberg, D. N. and Holland, P. R.: The Relative Impacts of Initialization and Climate Forcing in Coupled Ice Sheet-Ocean Modeling: Application to Pope, Smith, and Kohler Glaciers, *Journal of Geophysical Research: Earth Surface*, 127, e2021JF006570, <https://doi.org/10.1029/2021JF006570>, 2022.
- Goldberg, D. N., Gourmelen, N., Kimura, S., Millan, R., and Snow, K.: How Accurately Should We Model Ice Shelf Melt Rates?, *Geophysical Research Letters*, 46, 189–199, <https://doi.org/10.1029/2018GL080383>, 2019.
- 1120 Goldberg, D. N., Smith, T. A., Narayanan, S. H. K., Heimbach, P., and Morlighem, M.: Bathymetric Influences on Antarctic Ice-Shelf Melt Rates, *Journal of Geophysical Research: Oceans*, 125, e2020JC016370, <https://doi.org/10.1029/2020JC016370>, 2020.
- Gourmelen, N., Goldberg, D. N., Snow, K., Henley, S. F., Bingham, R. G., Kimura, S., Hogg, A. E., Shepherd, A., Mouginot, J., Lenaerts, J. T. M., Ligtenberg, S. R. M., and Berg, W. J. v. d.: Channelized Melting Drives Thinning Under a Rapidly Melting Antarctic Ice Shelf, *Geophysical Research Letters*, 44, 9796–9804, <https://doi.org/10.1002/2017GL074929>, 2017.
- 1125 Gudmundsson, G. H., Paolo, F. S., Adusumilli, S., and Fricker, H. A.: Instantaneous Antarctic ice sheet mass loss driven by thinning ice shelves, *Geophysical Research Letters*, 46, 13 903–13 909, <https://doi.org/10.1029/2019GL085027>, 2019.
- Hattermann, T., Nicholls, K. W., Hellmer, H. H., Davis, P. E. D., Janout, M. A., Østerhus, S., Schlosser, E., Rohardt, G., and Kanzow, T.: Observed interannual changes beneath Filchner-Ronne Ice Shelf linked to large-scale atmospheric circulation, *Nature Communications*, 12, 2961, <https://doi.org/10.1038/s41467-021-23131-x>, 2021.
- 1130 Hausmann, U., Sallée, J.-B., Jourdain, N. C., Mathiot, P., Rousset, C., Madec, G., Deshayes, J., and Hattermann, T.: The Role of Tides in Ocean-Ice Shelf Interactions in the Southwestern Weddell Sea, *Journal of Geophysical Research: Oceans*, 125, e2019JC015847, <https://doi.org/10.1029/2019JC015847>, 2020.
- Hersbach, H., Bell, B., Berrisford, P., Hirahara, S., Horányi, A., Muñoz-Sabater, J., Nicolas, J., Peubey, C., Radu, R., Schepers, D., Simmons, A., Soci, C., Abdalla, S., Abellan, X., Balsamo, G., Bechtold, P., Biavati, G., Bidlot, J., Bonavita, M., De Chiara, G., Dahlgren, P., Dee, D., Diamantakis, M., Dragani, R., Flemming, J., Forbes, R., Fuentes, M., Geer, A., Haimberger, L., Healy, S., Hogan, R. J., Hólm, E., Janisková, M., Keeley, S., Laloyaux, P., Lopez, P., Lupu, C., Radnoti, G., de Rosnay, P., Rozum, I., Vamborg, F., Villaume, S., and Thépaut, J.-N.: The ERA5 global reanalysis, *Quarterly Journal of the Royal Meteorological Society*, 146, 1999–2049, <https://doi.org/10.1002/qj.3803>, 2020.
- 1135 Hewitt, H., Fox-Kemper, B., Pearson, B., Roberts, M., and Klocke, D.: The small scales of the ocean may hold the key to surprises, *Nature Climate Change*, 12, 496–499, <https://doi.org/10.1038/s41558-022-01386-6>, 2022.
- Hewitt, I. J.: Subglacial Plumes, *Annual Review of Fluid Mechanics*, 52, 145–169, <https://doi.org/10.1146/annurev-fluid-010719-060252>, 2020.
- Holland, D. M. and Jenkins, A.: Modeling Thermodynamic Ice–Ocean Interactions at the Base of an Ice Shelf, *Journal of Physical Oceanography*, 29, 1787–1800, [https://doi.org/10.1175/1520-0485\(1999\)029<1787:MTIOIA>2.0.CO;2](https://doi.org/10.1175/1520-0485(1999)029<1787:MTIOIA>2.0.CO;2), 1999.

- 1145 Holland, D. M. and Jenkins, A.: Adaptation of an Isopycnic Coordinate Ocean Model for the Study of Circulation beneath Ice Shelves, *Monthly Weather Review*, 129, 1905–1927, [https://doi.org/10.1175/1520-0493\(2001\)129<1905:AOAICO>2.0.CO;2](https://doi.org/10.1175/1520-0493(2001)129<1905:AOAICO>2.0.CO;2), 2001.
- Holland, P. R. and Feltham, D. L.: Frazil dynamics and precipitation in a water column with depth-dependent supercooling, *Journal of Fluid Mechanics*, 530, 101–124, <https://doi.org/10.1017/S002211200400285X>, 2005.
- Holland, P. R. and Feltham, D. L.: The Effects of Rotation and Ice Shelf Topography on Frazil-Laden Ice Shelf Water Plumes, *Journal of Physical Oceanography*, 36, 2312–2327, <https://doi.org/10.1175/JPO2970.1>, 2006.
- 1150 Holland, P. R., Feltham, D. L., and Jenkins, A.: Ice Shelf Water plume flow beneath Filchner-Ronne Ice Shelf, Antarctica, *Journal of Geophysical Research: Oceans*, 112, <https://doi.org/10.1029/2006JC003915>, 2007.
- Holland, P. R., Corr, H. F. J., Vaughan, D. G., Jenkins, A., and Skvarca, P.: Marine ice in Larsen Ice Shelf, *Geophysical Research Letters*, 36, <https://doi.org/10.1029/2009GL038162>, 2009.
- 1155 Jenkins, A.: A one-dimensional model of ice shelf-ocean interaction, *Journal of Geophysical Research: Oceans*, 96, 20671–20677, <https://doi.org/10.1029/91JC01842>, 1991.
- Jenkins, A.: Convection-Driven Melting near the Grounding Lines of Ice Shelves and Tidewater Glaciers, *Journal of Physical Oceanography*, 41, 2279–2294, <https://doi.org/10.1175/JPO-D-11-03.1>, 2011.
- Jenkins, A., Corr, H. F. J., Nicholls, K. W., Stewart, C. L., and Doake, C. S. M.: Interactions between ice and  
1160 ocean observed with phase-sensitive radar near an Antarctic ice-shelf grounding line, *Journal of Glaciology*, 52, 325–346, <https://doi.org/10.3189/172756506781828502>, 2006.
- Jenkins, A., Nicholls, K. W., and Corr, H. F. J.: Observation and Parameterization of Ablation at the Base of Ronne Ice Shelf, Antarctica, *Journal of Physical Oceanography*, 40, 2298–2312, <https://doi.org/10.1175/2010JPO4317.1>, 2010.
- Jenkins, A., Shoosmith, D., Dutrieux, P., Jacobs, S., Kim, T. W., Lee, S. H., Ha, H. K., and Stammerjohn, S.: West Antarctic Ice Sheet retreat  
1165 in the Amundsen Sea driven by decadal oceanic variability, *Nature Geoscience*, 11, 733–738, <https://doi.org/10.1038/s41561-018-0207-4>, 2018.
- Jordan, J. R., Holland, P. R., Jenkins, A., Piggott, M. D., and Kimura, S.: Modeling ice-ocean interaction in ice-shelf crevasses, *Journal of Geophysical Research: Oceans*, 119, 995–1008, <https://doi.org/10.1002/2013JC009208>, 2014.
- Jordan, J. R., Holland, P. R., Goldberg, D., Snow, K., Arthern, R., Campin, J.-M., Heimbach, P., and Jenkins, A.: Ocean-Forced  
1170 Ice-Shelf Thinning in a Synchronously Coupled Ice-Ocean Model, *Journal of Geophysical Research: Oceans*, 123, 864–882, <https://doi.org/10.1002/2017JC013251>, 2018.
- Jourdain, N. C., Mathiot, P., Merino, N., Durand, G., Sommer, J. L., Spence, P., Dutrieux, P., and Madec, G.: Ocean circulation and sea-ice thinning induced by melting ice shelves in the Amundsen Sea, *Journal of Geophysical Research: Oceans*, 122, 2550–2573, <https://doi.org/10.1002/2016JC012509>, 2017.
- 1175 Jourdain, N. C., Asay-Davis, X., Hattermann, T., Straneo, F., Seroussi, H., Little, C. M., and Nowicki, S.: A protocol for calculating basal melt rates in the ISMIP6 Antarctic ice sheet projections, *The Cryosphere*, 14, 3111–3134, <https://doi.org/10.5194/tc-14-3111-2020>, 2020.
- Khazendar, A. and Jenkins, A.: A model of marine ice formation within Antarctic ice shelf rifts, *Journal of Geophysical Research: Oceans*, 108, <https://doi.org/10.1029/2002JC001673>, [\\_eprint: https://onlinelibrary.wiley.com/doi/pdf/10.1029/2002JC001673](https://onlinelibrary.wiley.com/doi/pdf/10.1029/2002JC001673), 2003.
- Khazendar, A., Rignot, E., Schroeder, D. M., Seroussi, H., Schodlok, M. P., Scheuchl, B., Mouginot, J., Sutterley, T. C., and Velicogna,  
1180 I.: Rapid submarine ice melting in the grounding zones of ice shelves in West Antarctica, *Nature Communications*, 7, 13243, <https://doi.org/10.1038/ncomms13243>, 2016.

- Killworth, P. D. and Edwards, N. R.: A Turbulent Bottom Boundary Layer Code for Use in Numerical Ocean Models, *Journal of Physical Oceanography*, 29, 1221–1238, [https://doi.org/10.1175/1520-0485\(1999\)029<1221:ATBBLC>2.0.CO;2](https://doi.org/10.1175/1520-0485(1999)029<1221:ATBBLC>2.0.CO;2), publisher: American Meteorological Society Section: *Journal of Physical Oceanography*, 1999.
- 1185 Kimura, S., Jenkins, A., Regan, H., Holland, P. R., Assmann, K. M., Whitt, D. B., Wessem, M. V., Berg, W. J. v. d., Reijmer, C. H., and Dutrieux, P.: Oceanographic Controls on the Variability of Ice-Shelf Basal Melting and Circulation of Glacial Meltwater in the Amundsen Sea Embayment, Antarctica, *Journal of Geophysical Research: Oceans*, 122, 10 131–10 155, <https://doi.org/10.1002/2017JC012926>, 2017.
- Large, W. G. and Yeager, S. G.: The global climatology of an interannually varying air–sea flux data set, *Climate Dynamics*, 33, 341–364, <https://doi.org/10.1007/s00382-008-0441-3>, 2009.
- 1190 Lazeroms, W. M. J., Jenkins, A., Rienstra, S. W., and Wal, R. S. W. v. d.: An Analytical Derivation of Ice-Shelf Basal Melt Based on the Dynamics of Meltwater Plumes, *Journal of Physical Oceanography*, 49, 917–939, <https://doi.org/10.1175/JPO-D-18-0131.1>, 2019.
- Lhermitte, S., Sun, S., Shuman, C., Wouters, B., Pattyn, F., Wuite, J., Berthier, E., and Nagler, T.: Damage accelerates ice shelf instability and mass loss in Amundsen Sea Embayment, *Proceedings of the National Academy of Sciences*, 117, 24 735–24 741, <https://doi.org/10.1073/pnas.1912890117>, 2020.
- 1195 Lilien, D. A., Joughin, I., Smith, B., and Gourmelen, N.: Melt at grounding line controls observed and future retreat of Smith, Pope, and Kohler glaciers, *The Cryosphere*, 13, 2817–2834, <https://doi.org/10.5194/tc-13-2817-2019>, 2019.
- MacAyeal, D. R., Rignot, E., and Hulbe, C. L.: Ice-shelf dynamics near the front of the Filchner-Ronne Ice Shelf, Antarctica, revealed by SAR interferometry: model/interferogram comparison, *Journal of Glaciology*, 44, 419–428, <https://doi.org/10.3189/S0022143000002744>, 1998.
- 1200 Madec, G., Bourdallé-Badie, R., Chanut, J., Clementi, E., Coward, A., Ethé, C., Iovino, D., Lea, D., Lévy, C., Lovato, T., Martin, N., Masson, S., Mocavero, S., Rousset, C., Storkey, D., Vancoppenolle, M., Müller, S., Nurser, G., Bell, M., and Samson, G.: NEMO ocean engine, <https://doi.org/10.5281/ZENODO.1464816>, 2019.
- Makinson, K., Holland, P. R., Jenkins, A., Nicholls, K. W., and Holland, D. M.: Influence of tides on melting and freezing beneath Filchner-Ronne Ice Shelf, Antarctica, *Geophysical Research Letters*, 38, <https://doi.org/10.1029/2010GL046462>, 2011.
- 1205 Marsh, O. J., Fricker, H. A., Siegfried, M. R., Christianson, K., Nicholls, K. W., Corr, H. F. J., and Catania, G.: High basal melting forming a channel at the grounding line of Ross Ice Shelf, Antarctica, *Geophysical Research Letters*, 43, 250–255, <https://doi.org/10.1002/2015GL066612>, 2016.
- Mathiot, P., Jenkins, A., Harris, C., and Madec, G.: Explicit representation and parametrised impacts of under ice shelf seas in the  $z^*$  coordinate ocean model NEMO 3.6, *Geoscientific Model Development*, 10, 2849–2874, <https://doi.org/10.5194/gmd-10-2849-2017>, 2017.
- 1210 Milillo, P., Rignot, E., Rizzoli, P., Scheuchl, B., Mouginot, J., Bueso-Bello, J. L., Prats-Iraola, P., and Dini, L.: Rapid glacier retreat rates observed in West Antarctica, *Nature Geoscience*, 15, 48–53, <https://doi.org/10.1038/s41561-021-00877-z>, 2022.
- Millgate, T., Holland, P. R., Jenkins, A., and Johnson, H. L.: The effect of basal channels on oceanic ice-shelf melting, *Journal of Geophysical Research: Oceans*, 118, 6951–6964, <https://doi.org/10.1002/2013JC009402>, 2013.
- Moholdt, G., Padman, L., and Fricker, H. A.: Basal mass budget of Ross and Filchner-Ronne ice shelves, Antarctica, derived from Lagrangian analysis of ICESat altimetry, *Journal of Geophysical Research: Earth Surface*, 119, 2361–2380, <https://doi.org/10.1002/2014JF003171>, 2014.
- Moorman, R., Morrison, A. K., and Hogg, A. M.: Thermal Responses to Antarctic Ice Shelf Melt in an Eddy-Rich Global Ocean–Sea Ice Model, *Journal of Climate*, 33, 6599–6620, <https://doi.org/10.1175/JCLI-D-19-0846.1>, 2020.

- Morlighem, M., Rignot, E., Binder, T., Blankenship, D., Drews, R., Eagles, G., Eisen, O., Ferraccioli, F., Forsberg, R., Fretwell, P., Goel, V., Greenbaum, J. S., Gudmundsson, H., Guo, J., Helm, V., Hofstede, C., Howat, I., Humbert, A., Jokat, W., Karlsson, N. B., Lee, W. S., Matsuoka, K., Millan, R., Mouginot, J., Paden, J., Pattyn, F., Roberts, J., Rosier, S., Ruppel, A., Seroussi, H., Smith, E. C., Steinhage, D., Sun, B., Broeke, M. R. v. d., Ommen, T. D. v., Wessem, M. v., and Young, D. A.: Deep glacial troughs and stabilizing ridges unveiled beneath the margins of the Antarctic ice sheet, *Nature Geoscience*, 13, 132–137, <https://doi.org/10.1038/s41561-019-0510-8>, 2020.
- Morrison, A. K., Hogg, A. M., England, M. H., and Spence, P.: Warm Circumpolar Deep Water transport toward Antarctica driven by local dense water export in canyons, *Science Advances*, 6, eaav2516, <https://doi.org/10.1126/sciadv.aav2516>, 2020.
- Nakayama, Y., Manucharyan, G., Zhang, H., Dutrieux, P., Torres, H. S., Klein, P., Seroussi, H., Schodlok, M., Rignot, E., and Menemenlis, D.: Pathways of ocean heat towards Pine Island and Thwaites grounding lines, *Scientific Reports*, 9, 16 649, <https://doi.org/10.1038/s41598-019-53190-6>, 2019.
- Nakayama, Y., Greene, C. A., Paolo, F. S., Mensah, V., Zhang, H., Kashiwase, H., Simizu, D., Greenbaum, J. S., Blankenship, D. D., Abe-Ouchi, A., and Aoki, S.: Antarctic Slope Current Modulates Ocean Heat Intrusions Towards Totten Glacier, *Geophysical Research Letters*, 48, e2021GL094 149, <https://doi.org/10.1029/2021GL094149>, 2021.
- Naughten, K. A., De Rydt, J., Rosier, S. H. R., Jenkins, A., Holland, P. R., and Ridley, J. K.: Two-timescale response of a large Antarctic ice shelf to climate change, *Nature Communications*, 12, 1991, <https://doi.org/10.1038/s41467-021-22259-0>, 2021.
- Naughten, K. A., Holland, P. R., Dutrieux, P., Kimura, S., Bett, D. T., and Jenkins, A.: Simulated Twentieth-Century Ocean Warming in the Amundsen Sea, West Antarctica, *Geophysical Research Letters*, 49, e2021GL094 566, <https://doi.org/10.1029/2021GL094566>, 2022.
- Nicholls, K. W., Østerhus, S., Makinson, K., Gammelsrød, T., and Fahrbach, E.: Ice-ocean processes over the continental shelf of the southern Weddell Sea, Antarctica: A review, *Reviews of Geophysics*, 47, <https://doi.org/10.1029/2007RG000250>, 2009.
- Oppenheimer, M., Glavovic, B., Hinkel, J., van de Wal, R., Magnan, A., Abd-Elgawad, A., Cai, R., Cifuentes-Jara, M., DeConto, R., Ghosh, T., Hay, J., Isla, F., Marzeion, B., Meyssignac, B., and Sebesvari, Z.: Sea Level Rise and Implications for Low-Lying Islands, Coasts and Communities, in: IPCC Special Report on the Ocean and Cryosphere in a Changing Climate, pp. 321–445, Cambridge University Press, Cambridge, UK and New York, NY, USA, <https://doi.org/10.1017/9781009157964.006>, [H.-O. Pörtner, D.C. Roberts, V. Masson-Delmotte, P. Zhai, M. Tignor, E. Poloczanska, K. Mintenbeck, A. Alegría, M. Nicolai, A. Okem, J. Petzold, B. Rama, N.M. Weyer (eds.)], 2019.
- Padman, L., Siegfried, M. R., and Fricker, H. A.: Ocean Tide Influences on the Antarctic and Greenland Ice Sheets, *Reviews of Geophysics*, 56, 142–184, <https://doi.org/10.1002/2016RG000546>, 2018.
- Payne, A. J., Holland, P. R., Shepherd, A. P., Rutt, I. C., Jenkins, A., and Joughin, I.: Numerical modeling of ocean-ice interactions under Pine Island Bay’s ice shelf, *Journal of Geophysical Research: Oceans*, 112, <https://doi.org/10.1029/2006JC003733>, 2007.
- Pelle, T., Morlighem, M., and Bondzio, J. H.: Brief communication: PICOP, a new ocean melt parameterization under ice shelves combining PICO and a plume model, *The Cryosphere*, 13, 1043–1049, <https://doi.org/10.5194/tc-13-1043-2019>, 2019.
- Pelletier, C., Fichet, T., Goosse, H., Haubner, K., Helsen, S., Huot, P.-V., Kittel, C., Klein, F., Le clec’h, S., van Lipzig, N. P. M., Marchi, S., Massonnet, F., Mathiot, P., Moravveji, E., Moreno-Chamarro, E., Ortega, P., Pattyn, F., Souverijns, N., Van Achter, G., Vanden Broucke, S., Vanhulle, A., Verfaillie, D., and Zipf, L.: PARASO, a circum-Antarctic fully coupled ice-sheet–ocean–sea-ice–atmosphere–land model involving f.ETISH1.7, NEMO3.6, LIM3.6, COSMO5.0 and CLM4.5, *Geoscientific Model Development*, 15, 553–594, <https://doi.org/10.5194/gmd-15-553-2022>, 2022.
- Reese, R., Albrecht, T., Mengel, M., Asay-Davis, X., and Winkelmann, R.: Antarctic sub-shelf melt rates via PICO, *The Cryosphere*, 12, 1969–1985, <https://doi.org/10.5194/tc-12-1969-2018>, 2018a.

- Reese, R., Gudmundsson, G. H., Levermann, A., and Winkelmann, R.: The far reach of ice-shelf thinning in Antarctica, *Nature Climate Change*, 8, 53–57, <https://doi.org/10.1038/s41558-017-0020-x>, 2018b.
- 1260 Richter, O., Gwyther, D. E., Galton-Fenzi, B. K., and Naughten, K. A.: The Whole Antarctic Ocean Model (WAOM v1.0): development and evaluation, *Geoscientific Model Development*, 15, 617–647, <https://doi.org/10.5194/gmd-15-617-2022>, 2022.
- Rignot, E. and Jacobs, S. S.: Rapid Bottom Melting Widespread near Antarctic Ice Sheet Grounding Lines, *Science*, 296, 2020–2023, <https://doi.org/10.1126/science.1070942>, 2002.
- Rignot, E., Jacobs, S., Mouginot, J., and Scheuchl, B.: Ice-Shelf Melting Around Antarctica, *Science*, 341, 266–270, <https://doi.org/10.1126/science.1235798>, 2013.
- 1265 Rosevear, M. G., Gayen, B., and Galton-Fenzi, B. K.: The role of double-diffusive convection in basal melting of Antarctic ice shelves, *Proceedings of the National Academy of Sciences*, 118, e2007541 118, <https://doi.org/10.1073/pnas.2007541118>, 2021.
- Rosevear, M. G., Gayen, B., and Galton-Fenzi, B. K.: Regimes and transitions in the basal melting of Antarctic ice shelves, *Journal of Physical Oceanography*, 1, <https://doi.org/10.1175/JPO-D-21-0317.1>, 2022.
- Sandhäger, H., Vaughan, D. G., and Lambrecht, A.: Meteoric, marine and total ice thickness maps of Filchner-Ronne-Schelfeis, Antarctica, p. 7, 2004.
- 1270 Scheuchl, B., Mouginot, J., Rignot, E., Morlighem, M., and Khazendar, A.: Grounding line retreat of Pope, Smith, and Kohler Glaciers, West Antarctica, measured with Sentinel-1a radar interferometry data, *Geophysical Research Letters*, 43, 8572–8579, <https://doi.org/10.1002/2016GL069287>, 2016.
- Schoof, C.: Ice sheet grounding line dynamics: Steady states, stability, and hysteresis, *Journal of Geophysical Research: Earth Surface*, 112, <https://doi.org/10.1029/2006JF000664>, 2007.
- 1275 Sergienko, O. V.: Basal channels on ice shelves, *Journal of Geophysical Research: Earth Surface*, 118, 1342–1355, <https://doi.org/10.1002/jgrf.20105>, 2013.
- Seroussi, H. and Morlighem, M.: Representation of basal melting at the grounding line in ice flow models, *The Cryosphere*, 12, 3085–3096, <https://doi.org/10.5194/tc-12-3085-2018>, 2018.
- 1280 Seroussi, H., Nowicki, S., Payne, A. J., Goelzer, H., Lipscomb, W. H., Abe-Ouchi, A., Agosta, C., Albrecht, T., Asay-Davis, X., Barthel, A., Calov, R., Cullather, R., Dumas, C., Galton-Fenzi, B. K., Gladstone, R., Gолledge, N. R., Gregory, J. M., Greve, R., Hattermann, T., Hoffman, M. J., Humbert, A., Huybrechts, P., Jourdain, N. C., Kleiner, T., Larour, E., Leguy, G. R., Lowry, D. P., Little, C. M., Morlighem, M., Pattyn, F., Pelle, T., Price, S. F., Quiquet, A., Reese, R., Schlegel, N.-J., Shepherd, A., Simon, E., Smith, R. S., Straneo, F., Sun, S., Trusel, L. D., Van Breedam, J., van de Wal, R. S. W., Winkelmann, R., Zhao, C., Zhang, T., and Zwinger, T.: ISMIP6 Antarctica: a multi-
- 1285 model ensemble of the Antarctic ice sheet evolution over the 21st century, *The Cryosphere*, 14, 3033–3070, <https://doi.org/10.5194/tc-14-3033-2020>, 2020.
- Shean, D. E., Joughin, I. R., Dutrieux, P., Smith, B. E., and Berthier, E.: Ice shelf basal melt rates from a high-resolution digital elevation model (DEM) record for Pine Island Glacier, Antarctica, *The Cryosphere*, 13, 2633–2656, <https://doi.org/https://doi.org/10.5194/tc-13-2633-2019>, 2019.
- 1290 Siahhan, A., Smith, R. S., Holland, P. R., Jenkins, A., Gregory, J. M., Lee, V., Mathiot, P., Payne, A. J., Ridley, J. K., and Jones, C. G.: The Antarctic contribution to 21st-century sea-level rise predicted by the UK Earth System Model with an interactive ice sheet, *The Cryosphere*, 16, 4053–4086, <https://doi.org/10.5194/tc-16-4053-2022>, 2022.

- Smith, R. S., Mathiot, P., Siahhaan, A., Lee, V., Cornford, S. L., Gregory, J. M., Payne, A. J., Jenkins, A., Holland, P. R., Ridley, J. K., and Jones, C. G.: Coupling the U.K. Earth System Model to Dynamic Models of the Greenland and Antarctic Ice Sheets, *Journal of Advances in Modeling Earth Systems*, 13, e2021MS002520, <https://doi.org/10.1029/2021MS002520>, 2021.
- 1295 Stewart, C. L., Christoffersen, P., Nicholls, K. W., Williams, M. J. M., and Dowdeswell, J. A.: Basal melting of Ross Ice Shelf from solar heat absorption in an ice-front polynya, *Nature Geoscience*, 12, 435–440, <https://doi.org/10.1038/s41561-019-0356-0>, 2019.
- Sun, S., Cornford, S. L., Moore, J. C., Gladstone, R., and Zhao, L.: Ice shelf fracture parameterization in an ice sheet model, *The Cryosphere*, 11, 2543–2554, <https://doi.org/10.5194/tc-11-2543-2017>, 2017.
- 1300 Sun, S., Pattyn, F., Simon, E. G., Albrecht, T., Cornford, S., Calov, R., Dumas, C., Gillet-Chaulet, F., Goelzer, H., Golledge, N. R., Greve, R., Hoffman, M. J., Humbert, A., Kazmierczak, E., Kleiner, T., Leguy, G. R., Lipscomb, W. H., Martin, D., Morlighem, M., Nowicki, S., Pollard, D., Price, S., Quiquet, A., Seroussi, H., Schlemm, T., Sutter, J., Wal, R. S. W. v. d., Winkelmann, R., and Zhang, T.: Antarctic ice sheet response to sudden and sustained ice-shelf collapse (ABUMIP), *Journal of Glaciology*, 66, 891–904, <https://doi.org/10.1017/jog.2020.67>, 2020.
- 1305 Thompson, A. F., Stewart, A. L., Spence, P., and Heywood, K. J.: The Antarctic Slope Current in a Changing Climate, *Reviews of Geophysics*, 56, 741–770, <https://doi.org/10.1029/2018RG000624>, 2018.
- van der Linden, E. C., Le Bars, D., Lambert, E., and Drijfhout, S.: Antarctic contribution to future sea level from ice shelf basal melt as constrained by ice discharge observations, *The Cryosphere*, 17, 79–103, <https://doi.org/10.5194/tc-17-79-2023>, publisher: Copernicus GmbH, 2023.
- 1310 Wählin, A. K., Graham, A. G. C., Hogan, K. A., Queste, B. Y., Boehme, L., Larter, R. D., Pettit, E. C., Wellner, J., and Heywood, K. J.: Pathways and modification of warm water flowing beneath Thwaites Ice Shelf, West Antarctica, *Science Advances*, 7, eabd7254, <https://doi.org/10.1126/sciadv.abd7254>, 2021.
- Zeising, O., Steinhage, D., Nicholls, K. W., Corr, H. F. J., Stewart, C. L., and Humbert, A.: Basal melt of the southern Filchner Ice Shelf, Antarctica, *The Cryosphere*, 16, 1469–1482, <https://doi.org/10.5194/tc-16-1469-2022>, 2022.

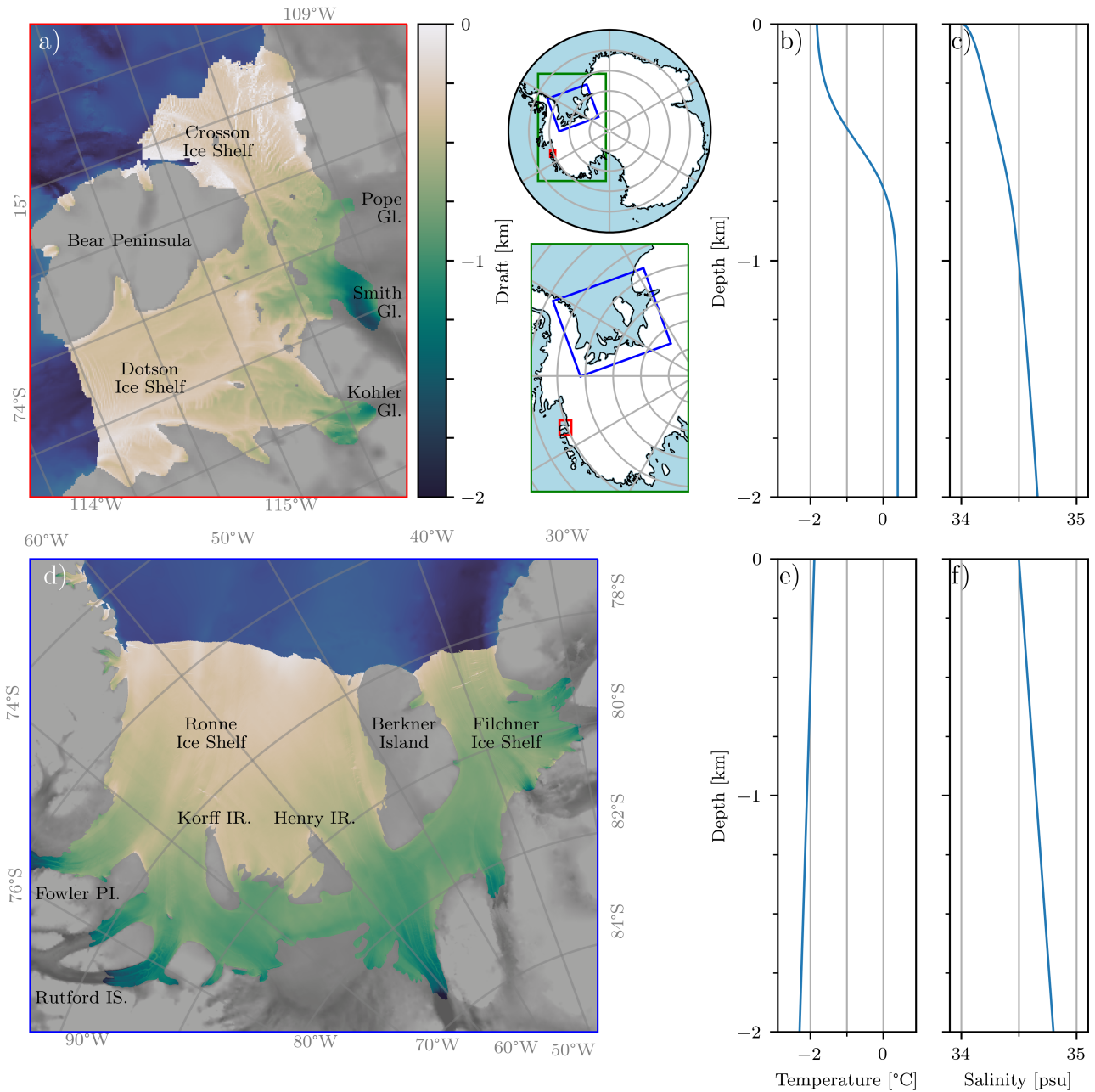


**Figure 2.** Geometry and forcing for the ~~Crosson-Dotson~~Crosson-Dotson and ~~Filchner-Ronne~~Filchner-Ronne Ice Shelves. a,b,d) Ice shelf geometries. The bright shading indicates the ice shelf draft, increasing from the grounding line to the ice-shelf front. The low-contrast shading denotes the bed topography below the open ocean (dark blue) and the grounded ice sheet (grey), with dark colours indicating a deep bed. The locations are indicated with the inset overview maps between a) and b). Abbreviations are: Gl. (Glacier), HIS. S.-(Ice Stream), KIR. IR.- (Korff Ice Rise), and HPI. I.R.- (Henry Ice Rise Peninsula). b,c,d,e,f) Idealised vertical temperature and salinity forcing profiles applied in the main simulations.

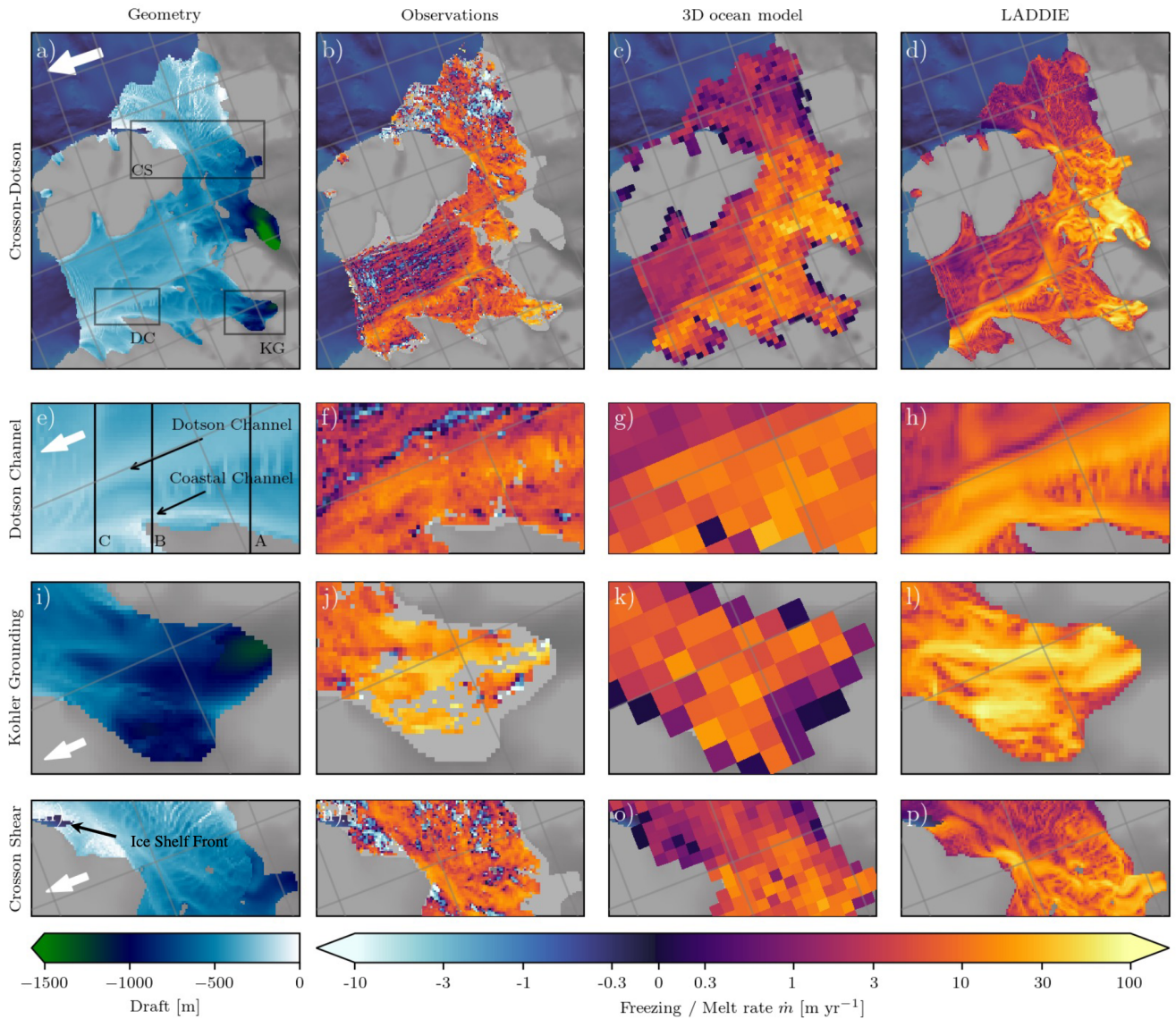
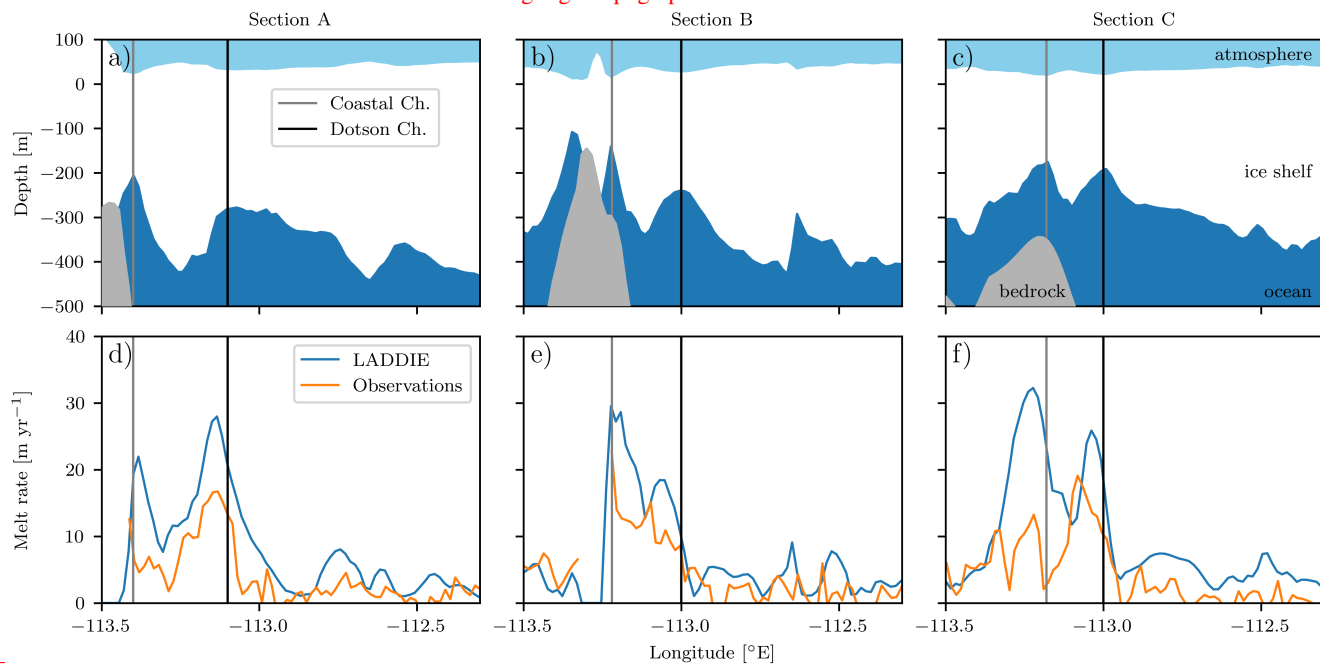


**Figure 3.** Spatial basal melt field of the ~~Crosson-Dotson~~ Crosson-Dotson Ice Shelf. a) Geometry in terms of ice shelf draft  $z_b$ . Details of the insets are shown in subsequent rows where DC is the Dotson Channel (shown in e–h), KG the Kohler Grounding zone (i–l), and CS the Crosson Shear margin (m–p). Place names are labelled in Fig. 2a and the white arrows point north. The sections indicated in e) are shown in Fig. 4 b) b) Observed basal melt rates from altimetry over the period 2010–2016 (Gourmelen et al., 2017; Goldberg et al., 2020). c) Basal melt rates from the 3D model MITgcm. d) Simulated basal melt rates using LADDIE. ~~The black contour line marks the ice shelf draft with a depth of 450 m~~ the vertical forcing profile shown in 2b–c. The melt colourscale is a symmetrical log-scale, and is linear between values  $-0.3$  and  $0.3 \text{ m yr}^{-1}$ . ~~The insets refer to KG (Kohler Grounding zone), DC (Dotson Channel), and CS (Crosson Shear margin); these regions are displayed in more detail in subsequent figures.~~

Kohler-grounding-zone-melt. Detailed features within the inset KG in Fig. ?? . Note the different colour scale for the ice shelf draft to

highlight topographic



details:

**Figure 4.** Cross sections across the Dotson and Coastal Channels. The location of sections A, B, and C are indicated in Fig. 3e. a-c) Geometry including the ice shelf (white), ocean cavity (blue), and solid earth (grey). The vertical lines indicate the topographic locations of the channel centerlines. d-f) Observed and simulated basal melt rates across the same sections.

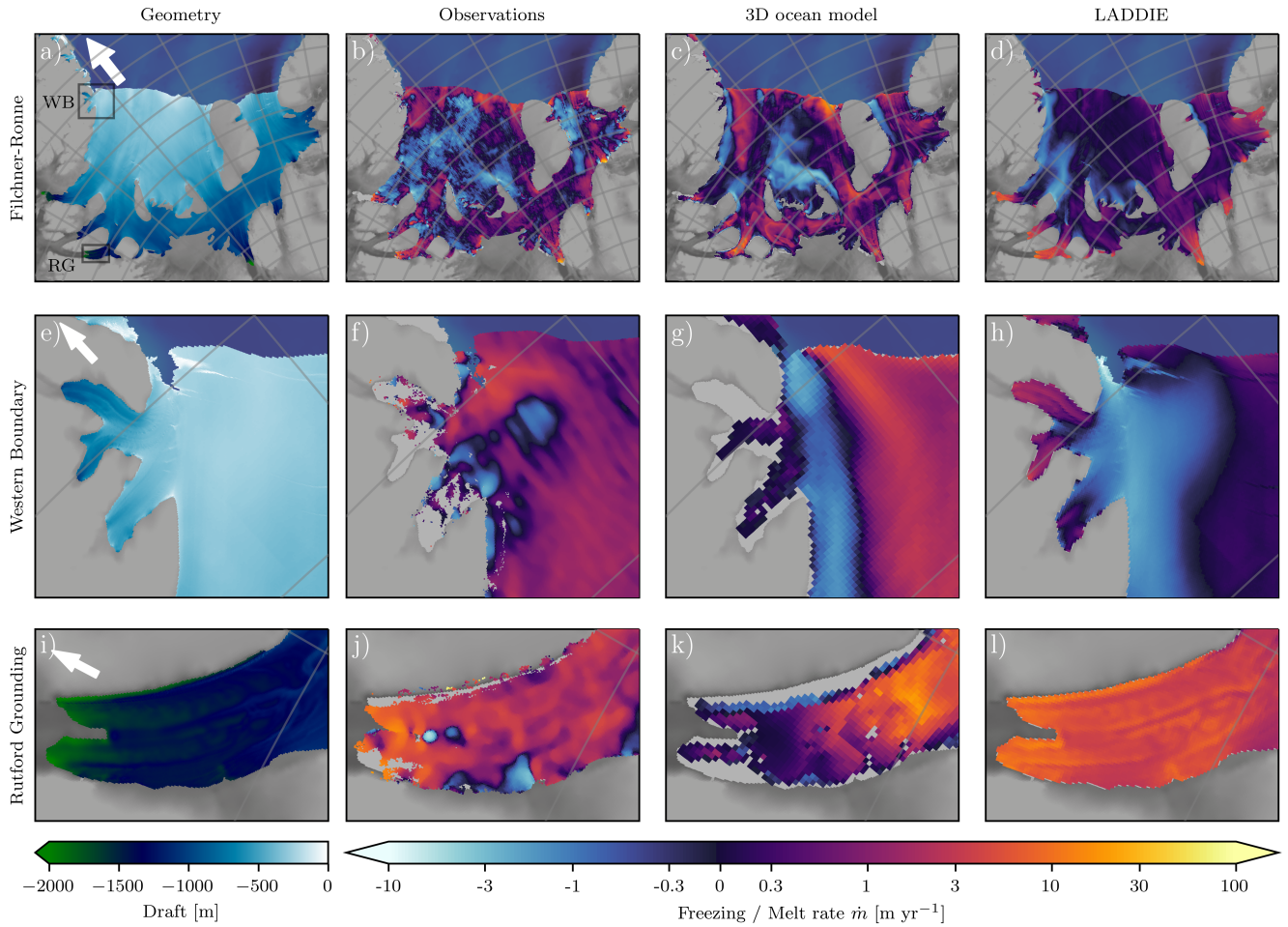


**Figure 5.** Spatial basal melt field of the Filchner-Ronne Ice Shelf. a) Geometry in terms of ice shelf draft. Insets shown in subsequent rows refer to the Western Boundary (WB, shown in e–h) and the Rutford Grounding zone (RG, shown in i–l). The white arrows point north. b) Observed basal melt rates from altimetry Adusumilli et al. (2020). c) Basal melt rates from the 3D model NEMO including tides Hausmann et al. (2020) (Hausmann et al., 2020). d) Simulated basal melt rates using LADDIE with the vertical forcing profile in Fig. WB: Western Boundary; RG: Rutford Grounding zone 2e–f.

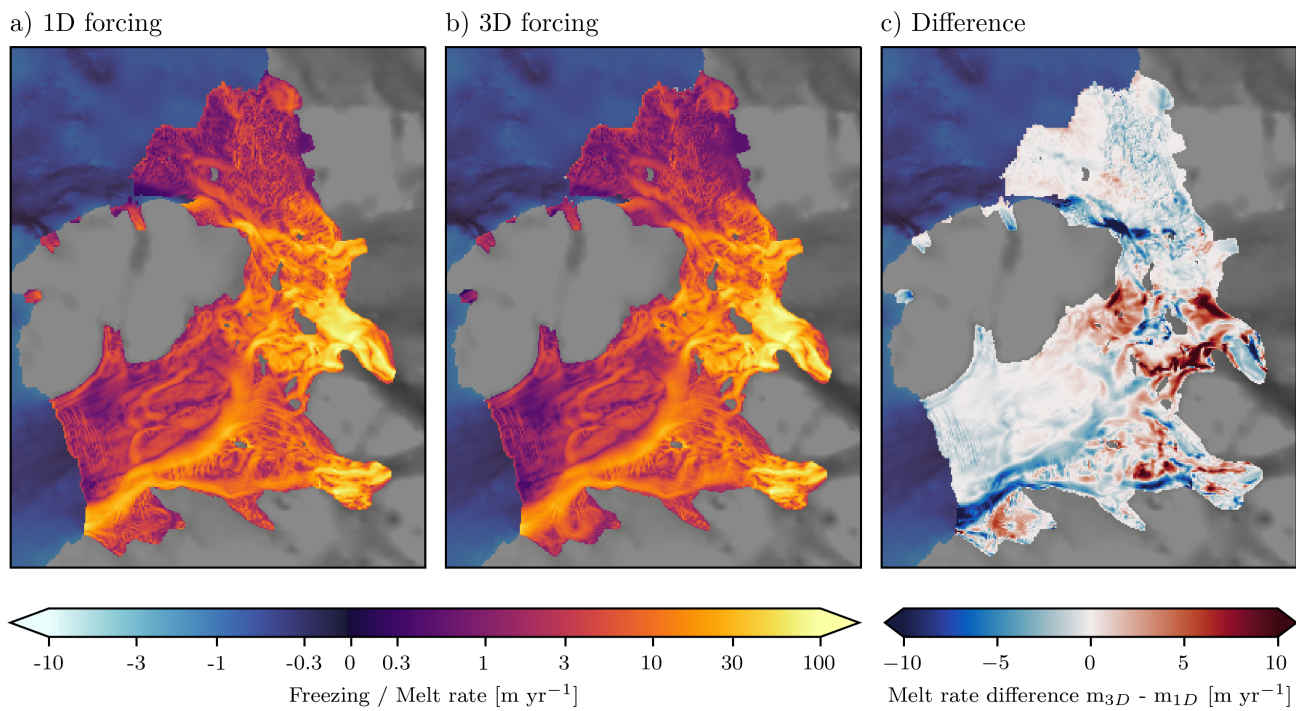


**Figure A1.** Impact of forcing on ~~Crosson-Dotson~~Crosson-Dotson melt rates. a) Melt rates from 1D forcing, identical to Fig. ~~???~~3d. b) Melt rates from 3D forcing. c) Difference between a) and b).

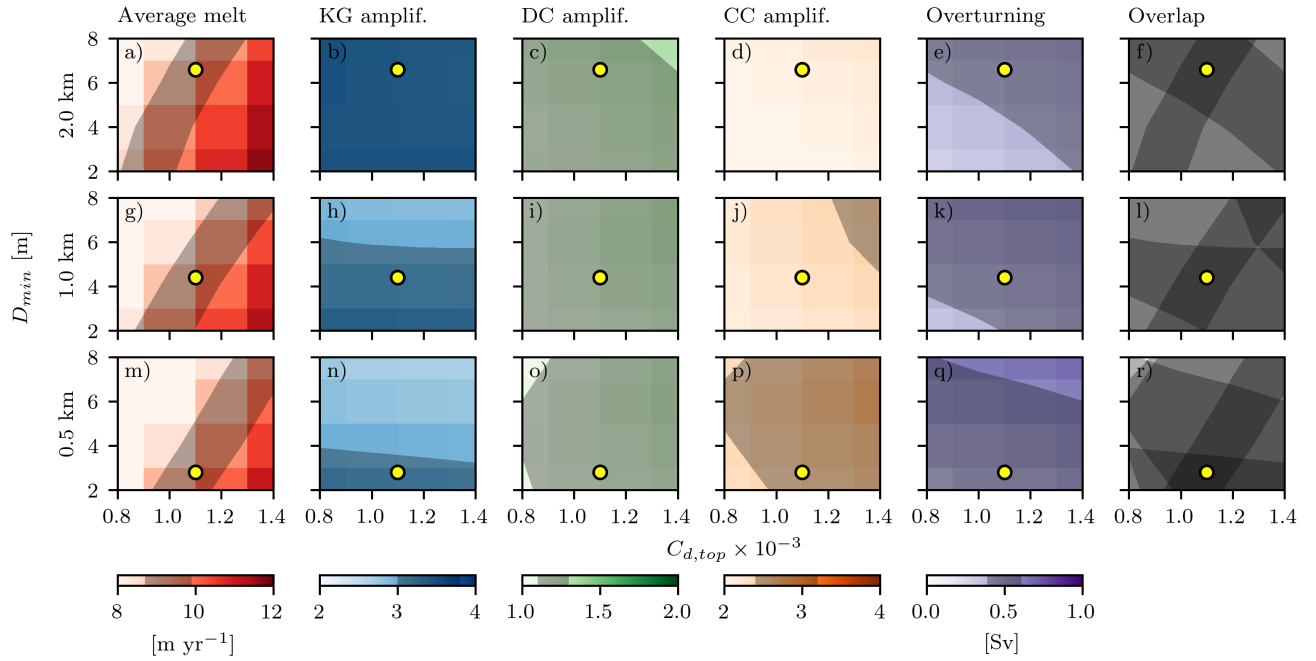


**Figure B1.** Parameter sensitivity test and tuning results. The three rows represent three horizontal resolutions (2.0, 1.0, and 0.5 km). Each column represents a diagnostic. Columns 2–4 denote the dimensionless melt amplification in the Kohler Grounding zone (KG), the Dotson Channel (DC) and along the Channel Centerline (CC). The grey shading denotes the tuning targets based on observations. The last column (Overlap) displays the overlap of these grey shaded regions, with darker colours indicating a better fit to observations. The yellow dots denote the chosen parameters for each resolution.

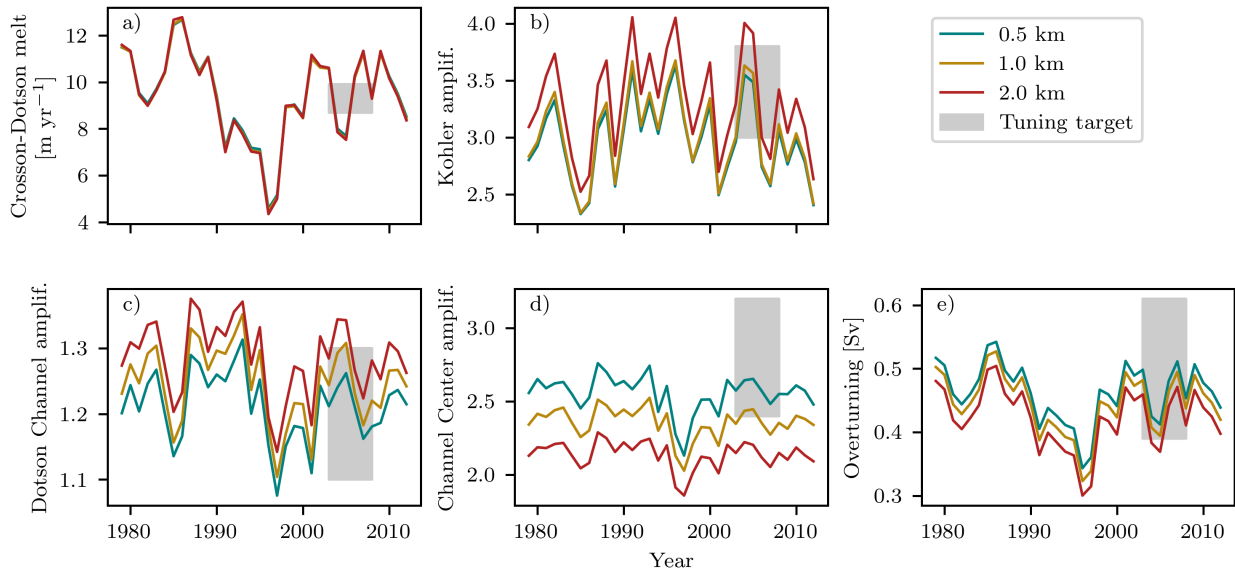


**Figure B2.** Time series of the main diagnostics for the ~~Crosson-Dotson~~ Crosson-Dotson Ice Shelf (the same as in Fig. B1). For each year, the annual mean temperature and salinity fields from MITgcm are used to force LADDIE until steady-state from a motionless initial state. The coloured lines again denote the different model resolutions. The grey regions denote the tuning targets, based on observations, applied to the period 2003–2008.

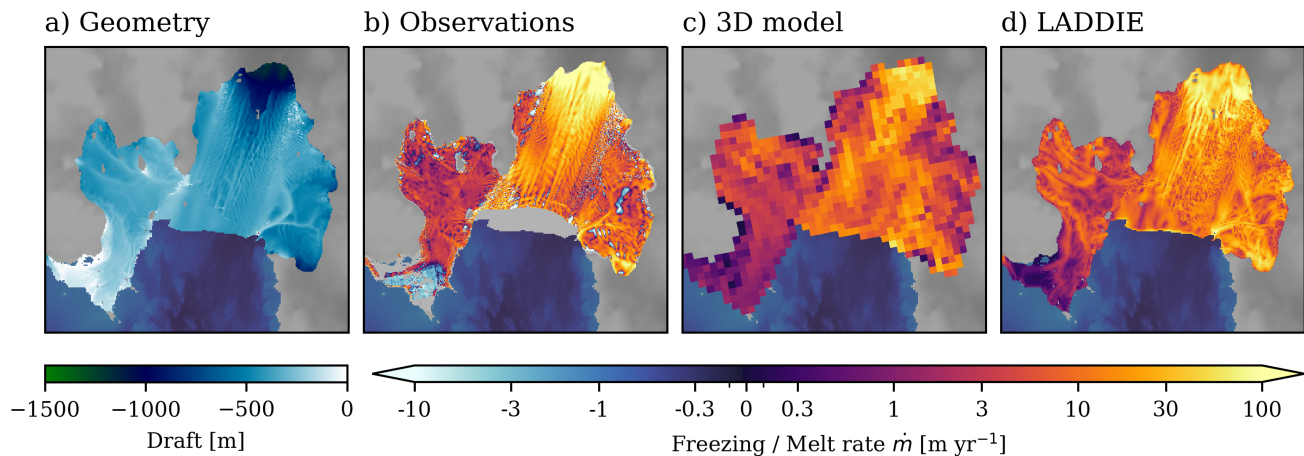


**Figure C1.** Geometry and basal melt for Pine Island Ice shelf. a) Geometry from BedMachine v2 (Morlighem et al., 2020). b) Observed basal melt rates from Shean et al. (2019). c) 3D model output from MITgcm (Sec 2.2.3). d) Results from LADDIE.